Model independent search for new phenomena in pp[over ¯] collisions at sqrt[s]=1.96 TeV

V. M. Abazov *et al.* (D0 Collaboration)

Model independent search for new phenomena in $p\bar{p}$ collisions at $\sqrt{s}$ =1.96 TeV

V.M. Abazov,[34] B. Abbott,[72] B.S. Acharya,[28] M. Adams,[48] T. Adams,[46] G.D. Alexeev,[34] G. Alkhazov,[38] A. Alton[a],[60] G. Alverson,[59] G.A. Alves,[2] M. Aoki,[47] M. Arov,[57] A. Askew,[46] B. Åsman,[40] S. Atkins,[57] O. Atramentov,[64] K. Augsten,[9] C. Avila,[7] J. BackusMayes,[79] F. Badaud,[12] L. Bagby,[47] B. Baldin,[47] D.V. Bandurin,[46] S. Banerjee,[28] E. Barberis,[59] P. Baringer,[55] J. Barreto,[3] J.F. Bartlett,[47] U. Bassler,[17] V. Bazterra,[48] A. Bean,[55] M. Begalli,[3] M. Begel,[70] C. Belanger-Champagne,[40] L. Bellantoni,[47] S.B. Beri,[26] G. Bernardi,[16] R. Bernhard,[21] I. Bertram,[41] M. Besançon,[17] R. Beuselinck,[42] V.A. Bezzubov,[37] P.C. Bhat,[47] V. Bhatnagar,[26] G. Blazey,[49] S. Blessing,[46] K. Bloom,[63] A. Boehnlein,[47] D. Boline,[69] E.E. Boos,[36] G. Borissov,[41] T. Bose,[58] A. Brandt,[75] O. Brandt,[22] R. Brock,[61] A. Brooijmans,[67] A. Bross,[47] D. Brown,[16] J. Brown,[16] X.B. Bu,[47] M. Buehler,[47] V. Buescher,[23] V. Bunichev,[36] S. Burdin[b],[41] T.H. Burnett,[79] C.P. Buszello,[40] B. Calpas,[14] E. Camacho-Pérez,[31] M.A. Carrasco-Lizarraga,[55] B.C.K. Casey,[47] H. Castilla-Valdez,[31] S. Chakrabarti,[69] D. Chakraborty,[49] K.M. Chan,[53] A. Chandra,[77] E. Chapon,[17] G. Chen,[55] S. Chevalier-Théry,[17] D.K. Cho,[74] S.W. Cho,[30] S. Choi,[30] B. Choudhary,[27] S. Cihangir,[47] D. Claes,[63] J. Clutter,[55] M. Cooke,[47] W.E. Cooper,[47] M. Corcoran,[77] F. Couderc,[17] M.-C. Cousinou,[14] A. Croc,[17] D. Cutts,[74] A. Das,[44] G. Davies,[42] K. De,[75] S.J. de Jong,[33] E. De La Cruz-Burelo,[31] F. Déliot,[17] M. Demarteau,[47] R. Demina,[68] D. Denisov,[47] S.P. Denisov,[37] S. Desai,[47] C. Deterre,[17] K. DeVaughan,[63] H.T. Diehl,[47] M. Diesburg,[47] P.F. Ding,[43] A. Dominguez,[63] T. Dorland,[79] A. Dubey,[27] L.V. Dudko,[36] D. Duggan,[64] A. Duperrin,[14] S. Dutt,[26] A. Dyshkant,[49] M. Eads,[63] D. Edmunds,[61] J. Ellison,[45] V.D. Elvira,[47] Y. Enari,[16] H. Evans,[51] A. Evdokimov,[70] V.N. Evdokimov,[37] G. Facini,[59] T. Ferbel,[68] F. Fiedler,[23] F. Filthaut,[33] W. Fisher,[61] H.E. Fisk,[47] M. Fortner,[49] H. Fox,[41] S. Fuess,[47] A. Garcia-Bellido,[68] G.A García-Guerra[c],[31] V. Gavrilov,[35] P. Gay,[12] W. Geng,[14, 61] D. Gerbaudo,[65] C.E. Gerber,[48] Y. Gershtein,[64] G. Ginther,[47, 68] G. Golovanov,[34] A. Goussiou,[79] P.D. Grannis,[69] S. Greder,[18] H. Greenlee,[47] Z.D. Greenwood,[57] E.M. Gregores,[4] G. Grenier,[19] Ph. Gris,[12] J.-F. Grivaz,[15] A. Grohsjean,[17] S. Grünendahl,[47] M.W. Grünewald,[29] T. Guillemin,[15] G. Gutierrez,[47] P. Gutierrez,[72] A. Haas[d],[67] S. Hagopian,[46] J. Haley,[59] L. Han,[6] K. Harder,[43] A. Harel,[68] J.M. Hauptman,[54] J. Hays,[42] T. Head,[43] T. Hebbeker,[20] D. Hedin,[49] H. Hegab,[73] A.P. Heinson,[45] U. Heintz,[74] C. Hensel,[22] I. Heredia-De La Cruz,[31] K. Herner,[60] G. Hesketh[e],[43] M.D. Hildreth,[53] R. Hirosky,[78] T. Hoang,[46] J.D. Hobbs,[69] B. Hoeneisen,[11] M. Hohlfeld,[23] Z. Hubacek,[9, 17] N. Huske,[16] V. Hynek,[9] I. Iashvili,[66] Y. Ilchenko,[76] R. Illingworth,[47] A.S. Ito,[47] S. Jabeen,[74] M. Jaffré,[15] D. Jamin,[14] A. Jayasinghe,[72] R. Jesik,[42] K. Johns,[44] M. Johnson,[47] A. Jonckheere,[47] P. Jonsson,[42] J. Joshi,[26] A.W. Jung,[47] A. Juste,[39] K. Kaadze,[56] E. Kajfasz,[14] D. Karmanov,[36] P.A. Kasper,[47] I. Katsanos,[63] R. Kehoe,[76] S. Kermiche,[14] N. Khalatyan,[47] A. Khanov,[73] A. Kharchilava,[66] Y.N. Kharzheev,[34] J.M. Kohli,[26] A.V. Kozelov,[37] J. Kraus,[61] S. Kulikov,[37] A. Kumar,[66] A. Kupco,[10] T. Kurča,[19] V.A. Kuzmin,[36] J. Kvita,[8] S. Lammers,[51] G. Landsberg,[74] P. Lebrun,[19] H.S. Lee,[30] S.W. Lee,[54] W.M. Lee,[47] J. Lellouch,[16] L. Li,[45] Q.Z. Li,[47] S.M. Lietti,[5] J.K. Lim,[30] D. Lincoln,[47] J. Linnemann,[61] V.V. Lipaev,[37] R. Lipton,[47] Y. Liu,[6] A. Lobodenko,[38] M. Lokajicek,[10] R. Lopes de Sa,[69] H.J. Lubatti,[79] R. Luna-Garcia[f],[31] A.L. Lyon,[47] A.K.A. Maciel,[2] D. Mackin,[77] R. Madar,[17] R. Magaña-Villalba,[31] P.K. Mal,[44] S. Malik,[63] V.L. Malyshev,[34] Y. Maravin,[56] J. Martínez-Ortega,[31] R. McCarthy,[69] C.L. McGivern,[55] M.M. Meijer,[33] A. Melnitchouk,[62] D. Menezes,[49] P.G. Mercadante,[4] M. Merkin,[36] A. Meyer,[20] J. Meyer,[22] F. Miconi,[18] N.K. Mondal,[28] G.S. Muanza,[14] M. Mulhearn,[78] E. Nagy,[14] M. Naimuddin,[27] M. Narain,[74] R. Nayyar,[27] H.A. Neal,[60] J.P. Negret,[7] P. Neustroev,[38] S.F. Novaes,[5] T. Nunnemann,[24] G. Obrant[‡],[38] J. Orduna,[77] N. Osman,[14] J. Osta,[53] G.J. Otero y Garzón,[1] M. Padilla,[45] A. Pal,[75] N. Parashar,[52] V. Parihar,[74] S.K. Park,[30] J. Parsons,[67] R. Partridge[d],[74] N. Parua,[51] A. Patwa,[70] B. Penning,[47] M. Perfilov,[36] K. Peters,[43] Y. Peters,[43] K. Petridis,[43] G. Petrillo,[68] P. Pétroff,[15] R. Piegaia,[1] J. Piper,[61] M.-A. Pleier,[70] P.L.M. Podesta-Lerma[g],[31] V.M. Podstavkov,[47] P. Polozov,[35] A.V. Popov,[37] M. Prewitt,[77] D. Price,[51] N. Prokopenko,[37] S. Protopopescu,[70] J. Qian,[60] A. Quadt,[22] B. Quinn,[62] M.S. Rangel,[2] K. Ranjan,[27] P.N. Ratoff,[41] I. Razumov,[37] P. Renkel,[76] M. Rijssenbeek,[69] I. Ripp-Baudot,[18] F. Rizatdinova,[73] M. Rominsky,[47] A. Ross,[41] C. Royon,[17] P. Rubinov,[47] R. Ruchti,[53] G. Safronov,[35] G. Sajot,[13] P. Salcido,[49] A. Sánchez-Hernández,[31] M.P. Sanders,[24] B. Sanghi,[47] A.S. Santos,[5] G. Savage,[47] L. Sawyer,[57] T. Scanlon,[42] R.D. Schamberger,[69] Y. Scheglov,[38] H. Schellman,[50] T. Schliephake,[25] S. Schlobohm,[79] C. Schwanenberger,[43] R. Schwienhorst,[61] J. Sekaric,[55] H. Severini,[72] E. Shabalina,[22] V. Shary,[17] A.A. Shchukin,[37] R.K. Shivpuri,[27] V. Simak,[9] V. Sirotenko,[47] P. Skubic,[72] P. Slattery,[68] D. Smirnov,[53] K.J. Smith,[66] G.R. Snow,[63] J. Snow,[71] S. Snyder,[70] S. Söldner-Rembold,[43] L. Sonnenschein,[20] K. Soustruznik,[8] J. Stark,[13] V. Stolin,[35] D.A. Stoyanova,[37]

M. Strauss,[72] D. Strom,[48] L. Stutte,[47] L. Suter,[43] P. Svoisky,[72] M. Takahashi,[43] A. Tanasijczuk,[1] M. Titov,[17]
V.V. Tokmenin,[34] Y.-T. Tsai,[68] K. Tschann-Grimm,[69] D. Tsybychev,[69] B. Tuchming,[17] C. Tully,[65] L. Uvarov,[38]
S. Uvarov,[38] S. Uzunyan,[49] R. Van Kooten,[51] W.M. van Leeuwen,[32] N. Varelas,[48] E.W. Varnes,[44] I.A. Vasilyev,[37]
P. Verdier,[19] L.S. Vertogradov,[34] M. Verzocchi,[47] M. Vesterinen,[43] D. Vilanova,[17] P. Vokac,[9] H.D. Wahl,[46]
M.H.L.S. Wang,[47] J. Warchol,[53] G. Watts,[79] M. Wayne,[53] M. Weber[h],[47] L. Welty-Rieger,[50] A. White,[75] D. Wicke,[25]
M.R.J. Williams,[41] G.W. Wilson,[55] M. Wobisch,[57] D.R. Wood,[59] T.R. Wyatt,[43] Y. Xie,[47] C. Xu,[60] S. Yacoob,[50]
R. Yamada,[47] W.-C. Yang,[43] T. Yasuda,[47] Y.A. Yatsunenko,[34] Z. Ye,[47] H. Yin,[47] K. Yip,[70] S.W. Youn,[47]
J. Yu,[75] S. Zelitch,[78] T. Zhao,[79] B. Zhou,[60] J. Zhu,[60] M. Zielinski,[68] D. Zieminska,[51] and L. Zivkovic[74]

(The D0 Collaboration[*])

[1]Universidad de Buenos Aires, Buenos Aires, Argentina
[2]LAFEX, Centro Brasileiro de Pesquisas Físicas, Rio de Janeiro, Brazil
[3]Universidade do Estado do Rio de Janeiro, Rio de Janeiro, Brazil
[4]Universidade Federal do ABC, Santo André, Brazil
[5]Instituto de Física Teórica, Universidade Estadual Paulista, São Paulo, Brazil
[6]University of Science and Technology of China, Hefei, People's Republic of China
[7]Universidad de los Andes, Bogotá, Colombia
[8]Charles University, Faculty of Mathematics and Physics,
Center for Particle Physics, Prague, Czech Republic
[9]Czech Technical University in Prague, Prague, Czech Republic
[10]Center for Particle Physics, Institute of Physics,
Academy of Sciences of the Czech Republic, Prague, Czech Republic
[11]Universidad San Francisco de Quito, Quito, Ecuador
[12]LPC, Université Blaise Pascal, CNRS/IN2P3, Clermont, France
[13]LPSC, Université Joseph Fourier Grenoble 1, CNRS/IN2P3,
Institut National Polytechnique de Grenoble, Grenoble, France
[14]CPPM, Aix-Marseille Université, CNRS/IN2P3, Marseille, France
[15]LAL, Université Paris-Sud, CNRS/IN2P3, Orsay, France
[16]LPNHE, Universités Paris VI and VII, CNRS/IN2P3, Paris, France
[17]CEA, Irfu, SPP, Saclay, France
[18]IPHC, Université de Strasbourg, CNRS/IN2P3, Strasbourg, France
[19]IPNL, Université Lyon 1, CNRS/IN2P3, Villeurbanne, France and Université de Lyon, Lyon, France
[20]III. Physikalisches Institut A, RWTH Aachen University, Aachen, Germany
[21]Physikalisches Institut, Universität Freiburg, Freiburg, Germany
[22]II. Physikalisches Institut, Georg-August-Universität Göttingen, Göttingen, Germany
[23]Institut für Physik, Universität Mainz, Mainz, Germany
[24]Ludwig-Maximilians-Universität München, München, Germany
[25]Fachbereich Physik, Bergische Universität Wuppertal, Wuppertal, Germany
[26]Panjab University, Chandigarh, India
[27]Delhi University, Delhi, India
[28]Tata Institute of Fundamental Research, Mumbai, India
[29]University College Dublin, Dublin, Ireland
[30]Korea Detector Laboratory, Korea University, Seoul, Korea
[31]CINVESTAV, Mexico City, Mexico
[32]Nikhef, Science Park, Amsterdam, the Netherlands
[33]Radboud University Nijmegen, Nijmegen, the Netherlands and Nikhef, Science Park, Amsterdam, the Netherlands
[34]Joint Institute for Nuclear Research, Dubna, Russia
[35]Institute for Theoretical and Experimental Physics, Moscow, Russia
[36]Moscow State University, Moscow, Russia
[37]Institute for High Energy Physics, Protvino, Russia
[38]Petersburg Nuclear Physics Institute, St. Petersburg, Russia
[39]Institució Catalana de Recerca i Estudis Avançats (ICREA) and Institut de Física d'Altes Energies (IFAE), Barcelona, Spain
[40]Stockholm University, Stockholm and Uppsala University, Uppsala, Sweden
[41]Lancaster University, Lancaster LA1 4YB, United Kingdom
[42]Imperial College London, London SW7 2AZ, United Kingdom
[43]The University of Manchester, Manchester M13 9PL, United Kingdom
[44]University of Arizona, Tucson, Arizona 85721, USA
[45]University of California Riverside, Riverside, California 92521, USA
[46]Florida State University, Tallahassee, Florida 32306, USA
[47]Fermi National Accelerator Laboratory, Batavia, Illinois 60510, USA
[48]University of Illinois at Chicago, Chicago, Illinois 60607, USA
[49]Northern Illinois University, DeKalb, Illinois 60115, USA
[50]Northwestern University, Evanston, Illinois 60208, USA

[51] *Indiana University, Bloomington, Indiana 47405, USA*
[52] *Purdue University Calumet, Hammond, Indiana 46323, USA*
[53] *University of Notre Dame, Notre Dame, Indiana 46556, USA*
[54] *Iowa State University, Ames, Iowa 50011, USA*
[55] *University of Kansas, Lawrence, Kansas 66045, USA*
[56] *Kansas State University, Manhattan, Kansas 66506, USA*
[57] *Louisiana Tech University, Ruston, Louisiana 71272, USA*
[58] *Boston University, Boston, Massachusetts 02215, USA*
[59] *Northeastern University, Boston, Massachusetts 02115, USA*
[60] *University of Michigan, Ann Arbor, Michigan 48109, USA*
[61] *Michigan State University, East Lansing, Michigan 48824, USA*
[62] *University of Mississippi, University, Mississippi 38677, USA*
[63] *University of Nebraska, Lincoln, Nebraska 68588, USA*
[64] *Rutgers University, Piscataway, New Jersey 08855, USA*
[65] *Princeton University, Princeton, New Jersey 08544, USA*
[66] *State University of New York, Buffalo, New York 14260, USA*
[67] *Columbia University, New York, New York 10027, USA*
[68] *University of Rochester, Rochester, New York 14627, USA*
[69] *State University of New York, Stony Brook, New York 11794, USA*
[70] *Brookhaven National Laboratory, Upton, New York 11973, USA*
[71] *Langston University, Langston, Oklahoma 73050, USA*
[72] *University of Oklahoma, Norman, Oklahoma 73019, USA*
[73] *Oklahoma State University, Stillwater, Oklahoma 74078, USA*
[74] *Brown University, Providence, Rhode Island 02912, USA*
[75] *University of Texas, Arlington, Texas 76019, USA*
[76] *Southern Methodist University, Dallas, Texas 75275, USA*
[77] *Rice University, Houston, Texas 77005, USA*
[78] *University of Virginia, Charlottesville, Virginia 22901, USA*
[79] *University of Washington, Seattle, Washington 98195, USA*

We describe a model independent search for physics beyond the standard model in lepton final states. We examine 117 final states using 1.1 fb^{-1} of $p\bar{p}$ collisions data at $\sqrt{s} = 1.96$ TeV collected with the D0 detector. We conclude that all observed discrepancies between data and model can be attributed to uncertainties in the standard model background modeling, and hence we do not see any evidence for physics beyond the standard model.

I. INTRODUCTION

The standard model (SM) has been remarkably successful in accommodating all the interactions between the fundamental particles [1]. Despite this success, there are strong motivations to expect new phenomena at energies at the order of the electroweak scale. For example, the Higgs boson [2] receives quantum corrections to its mass through loop diagrams. The scalar nature of the Higgs boson leads to a quadratic divergence, with an upper limit of the integral set by the highest scale, i.e., the Planck mass (10^{19} GeV). To maintain the Higgs mass close to the electroweak scale, it is necessary to fine tune a parameter in the theory to within $M_W/M_{\mathrm{Planck}} \approx 10^{-16}$

[3].

There are few logical options for overcoming this problem. If the Higgs boson does not exist, then there must be a new contribution to the physics at the electroweak scale. If the Higgs boson does exist, then the theory must be either fine tuned or a generalized Higgs scheme, beyond the SM, is present at the electroweak scale.

Assuming that beyond standard model (BSM) physics exists, we do not know how it appears, rendering its search difficult. While there are many theories that predict observable differences with the SM, these models usually depend on additional unspecified parameters which broaden the possible range of results.

Motivated by uncertainty and expectations of physics beyond the SM, we examine data from many channels in $p\bar{p}$ collisions at $\sqrt{s} = 1.96$ TeV at the Tevatron Collider at Fermilab, collected by the D0 experiment, for deviations from the SM. After this, we focus on events with objects with high transverse momentum (p_T) in a quasi-model-independent search for new phenomena effects. Similar approaches have been applied to data from the D0 Collaboration [4–6], the H1 Collaboration at the HERA ep collider at DESY [7], and the CDF Collaboration at the

*with visitors from ^{a}Augustana College, Sioux Falls, SD, USA, ^{b}The University of Liverpool, Liverpool, UK, ^{c}UPIITA-IPN, Mexico City, Mexico, ^{c}SLAC, Menlo Park, CA, USA, ^{e}University College London, London, UK, ^{f}Centro de Investigacion en Computacion - IPN, Mexico City, Mexico, ^{g}ECFM, Universidad Autonoma de Sinaloa, Culiacán, Mexico, and ^{h}Universität Bern, Bern, Switzerland. ‡Deceased.

Tevatron [8, 9].

Our technique trades the sensitivity of specific searches for breadth of coverage: we do not design selections focused on a particular model and neglect systematic uncertainties. This way, we can incorporate many channels without developing a detailed modeling for each individual channel. This approach limits sensitivity for physics beyond the SM in individual final states, but it helps identify global differences relative to the SM expectations. If any particular final state or distribution found discrepant with the SM remains significantly discrepant after systematic uncertainties are considered, then it warrants claim for the presence of physics beyond the SM. The benefit of this approach is that we can look in a co-ordinated way at many channels, applying expectations from the SM and a model of the detector in a relatively straightforward manner, to search for discrepancies between data and the SM.

The data for this search consists of events containing high p_T objects. The SM background estimates are based on Monte Carlo (MC) predictions supplemented with data-driven estimates of backgrounds where a jet fakes a lepton (multijet backgrounds). We apply corrections to the MC simulation, determined either from previous D0 studies based on well-understood regions of phase space or from higher-order MC simulations. These corrections are discussed further in Sec. IV.

We divide the data and the selected MC simulated events into seven inclusive subsets based on the number and types of leptons identified in each event. Unlike the search conducted by the CDF Collaboration [8, 9], only events with at least one electron or muon are considered. To account for any incorrect normalizations in the absence of higher order corrections to the cross section calculations, and for experimental systematic uncertainties, we determine scale factors for the MC contributions by fitting kinematic distributions in each of the seven inclusive subsets, as discussed in Sec. V.

The seven non-overlapping inclusive subsets are merged to provide input for the analyses employing algorithms called VISTA and SLEUTH [8], as discussed in Sec. VII. In brief, VISTA searches for deviations in bulk distributions, while SLEUTH looks for excesses of data in the high-p_T tails.

II. D0 DETECTOR

The data correspond to 1.07 ± 0.07 fb^{-1} of integrated luminosity from $p\bar{p}$ collisions at the Tevatron Collider at Fermilab, collected with the D0 detector at $\sqrt{s} = 1.96$ TeV during 2002–2006.

The D0 detector is described in detail elsewhere [10]. The central tracking, calorimetry, and muon systems are the components most important to this analysis. The central tracking system consists of a silicon microstrip tracker (SMT) and a central fiber tracker (CFT), both located within a 2 T superconducting solenoidal magnet,

and provides charged particle tracking for pseudorapidities $|\eta| < 3$, where $\eta = -\ln[\tan(\theta/2)]$, and θ is the polar angle relative to the center of the detector with respect to the proton beam direction.

The three liquid-argon/uranium calorimeters are housed in separate cryostats. Outside of the tracking system, a central section covers up to $|\eta| = 1.1$. Two end calorimeters extend coverage to $|\eta| = 4.2$. The calorimeter is highly segmented with four electromagnetic (EM) and four to five hadronic longitudinal layers; transverse to the particle direction, typical segmentation is $\Delta\eta = \Delta\phi = 0.1$, where ϕ is the azimuthal angle.

Beyond the calorimeter, a muon system consists of a layer of tracking detectors and scintillation trigger counters in front of 1.8 T iron toroids, followed by two similar layers after the toroids, all at pseudorapidities $|\eta| < 2.0$ [11].

A three level trigger system selects events, recording data at about 100 Hz. Our sample was collected using triggers that select events with at least one electron or one muon. The same trigger requirements are applied in the selection of the data samples used for the estimation of the multijet backgrounds.

III. OBJECT ID AND EVENT SELECTION

In this section, we describe the identification criteria used to select energetic objects isolated from other event activity, *viz.*, electrons ($e^\pm$), muons ($\mu^\pm$), tau leptons ($\tau^\pm$), missing transverse energy ($\not{E}_T$), jets, and b-quark jets. In addition, we discuss the criteria used to select samples of non-isolated electrons and muons. These objects are used to estimate the contribution of instrumental backgrounds to our final states. Objects that pass very loose isolation criteria but fail the tighter isolation criteria used for our signal events are primarily from jets. Events with these objects passing very loose isolation criteria are kinematically similar to events where the jet successfully mimics an isolated lepton. The number of these events in each final state is determined as part of the inclusive normalization fits, detailed in Sec. VI.

A. Vertices

Only $p\bar{p}$ interaction vertices reconstructed from at least three tracks are allowed in this analysis. Based on the p_T of the tracks associated with that vertex, we define the primary $p\bar{p}$ interaction vertex (PV), as the one with smallest probability of originating from a minimum-bias interaction [12]. The z coordinate of the PV ($z_{\rm PV}$) is required to be $|z_{\rm PV}| < 60$ cm (where the positive z axis is oriented along the proton beam direction, with origin at the center of the detector).

B. Electrons

Electrons are characterized by an isolated shower in the calorimeter and an isolated track in the central tracker. Starting with a seed cell, a calorimeter cluster is formed using cells within a cone of radius $\Delta \mathcal{R} < 0.4$ where $\Delta \mathcal{R} = \sqrt{(\Delta \eta)^2 + (\Delta \phi)^2}$. Such clusters are required to pass the calorimeter isolation criterion $(E_{\text{tot}}(\Delta \mathcal{R} < 0.4) - E_{\text{EM}}(\Delta \mathcal{R} < 0.2))/E_{\text{EM}}(\Delta \mathcal{R} < 0.2) < 0.2$, where E_{tot} is the total energy of the shower, summing the EM and hadronic calorimeter cells, and E_{EM} is the energy in the EM calorimeter only. Every accepted cluster must have 90% of E_{tot} within the EM calorimeter, pass a χ^2-based selection on the spatial distribution of the shower, and be matched with a track extrapolated from the central tracker. An electron likelihood (L_e), based on seven tracking and calorimetric parameters, is used to enhance signal purity of the candidate electrons. Different selection criteria on L_e are used for different final states, as discussed in Sec. V.

In this analysis, we use only electrons that are found in the central calorimeter (CC), with $|\eta| < 1.1$ and $p_T > 15$ GeV. Typical electron detection efficiencies are 70% to 80%.

To estimate the contribution from non-isolated electrons (e.g. from multijet background), we use the same selection as for signal, but with a reversed L_e likelihood criterion.

C. Muons

Muons are identified in the muon system, and then matched to tracks. They are required to have $|\eta| < 1.5$ and $p_T > 15$ GeV. The track requirements include a selection on DCA < 0.02 (0.2) cm for tracks with (without) hits in the SMT, where DCA is the distance of closest approach of the track to the PV in the transverse plane.

We require muons to be isolated, meaning that the sum of the transverse energies in calorimeter cells in an annular region ($0.1 < \Delta \mathcal{R} < 0.4$) around the muon track, and the sum of the tracks p_T in a cone of $\Delta \mathcal{R} < 0.5$ around the muon track must both be less than 2.5 GeV.

To estimate the multijet background in the single muon sample, we use control samples where the isolation variables are required to be between 2.5 GeV and 8 GeV. All other criteria are the same as in the signal data sample.

Because the muon p_T is estimated by the p_T of the matching track in the central tracker, the momentum resolution decreases with increasing p_T. To restrict the analysis to muons with well measured momenta, we require the significance of its p_T measurement to be $(1/p_T)/\sigma(1/p_T) > 3$, where $\sigma(1/p_T)$ is the uncertainty on the measurement of the track curvature (inverse of the muon track's p_T). This effectively limits muons to $p_T < 200$ GeV.

D. Tau Leptons

Tau leptons can decay to $e\nu_e\nu_\tau$, $\mu\nu_\mu\nu_\tau$, or hadrons $h\nu_\tau$ (τ_h). It is difficult to determine whether a light lepton in an event originated from a τ, but the signature from $\tau_h \to h\nu_\tau$ differs significantly from that of a jet. The decays $\tau \to \pi\nu_\tau$ are referred to as Type-1. Decays corresponding to $\tau^\pm \to \pi^\pm n\pi^0 \nu_\tau$ are referred to as Type-2 (n is an integer ≥ 1), and decays to multiple charged pions are referred to as Type-3 decays. Type-3 decays differ from Type-1 (τ_1) and Type-2 (τ_2) by being matched to multiple tracks, and are not used in this analysis. Type-1 and Type-2 decays are required to have $|\eta| < 1.1$ and a track with at least one SMT hit, as well as $p_T > 10$ GeV for Type-1, and $p_T > 5$ GeV for Type-2 tau leptons. There are also requirements concerning overlaps of objects: $\Delta \mathcal{R}(\mu, \tau) > 0.4$ and $\Delta \mathcal{R}(e, \tau) > 0.4$, where τ, μ and e are as defined above, except that muons that pass the overlap criterion do not have to pass the additional isolation requirement. To distinguish τ_h decays from jets, we use a neural network discriminant [13], NN_h, and to distinguish Type-2 τ_h from electrons, we use an additional neural network, NN_e. We require $NN_h > 0.9$ for τ_1 and τ_2, and $NN_e > 0.2$ for τ_2.

To model the multijet contribution to final states with τ_h decays, we select events with τ_h candidates as above, but with $0.3 < NN_h < 0.8$.

E. Jets

We reconstruct jets within $|\eta| < 2.5$, using an iterative midpoint cone algorithm [14] with cone radius of 0.5 and a minimum p_T requirement of 20 GeV after applying a jet energy scale (JES) correction as discussed in Sec. IV B 3. Jets separated from a τ_h or an electron by $\Delta \mathcal{R} < 0.5$ are removed from consideration.

F. b-jets

Bottom and charm quarks can travel measurable distances from the PV before decaying, so that their decay products originate from an identifiable secondary vertex. This provides a way of tagging jets coming from a $b(c)$-quark decay by examining the associated tracks [15]. Before applying any b-tagging criteria, the jets are required to pass both calorimeter criteria outlined in Sec. III E and the taggability criteria. A jet is taggable if it is matched to a track jet, which is a jet formed from tracks, reconstructed using a simple cone-clustering algorithm of $\Delta \mathcal{R} < 0.5$. At least two tracks are required, with at least one having $p_T > 1$ GeV and another with $p_T > 0.5$ GeV. Every track in the jet is required to have at least one hit in the SMT detector, a DCA < 0.2 cm, and a distance of closest approach along the z axis of < 0.4 cm.

All taggable jets are subjected to a neural network b tagging algorithm [15] whose input variables include the

DCA of each track in a jet and information on secondary vertices in the jet. We define b-jet candidates by requiring that the neural network output be greater than 0.775. This algorithm selects about 60% of b jets with $p_T = 50$ GeV, and only 1% of light flavor (u, d, s quarks or gluon) jets.

G. Missing Transverse Energy

Neutrinos or other weakly-interacting neutral particles do not leave energy deposits in the detector. Their presence is inferred from the measurement of significant $\displaystyle{\not}E_T$ in the event. The missing transverse energy is determined from energies deposited in all calorimeter cells. The $\displaystyle{\not}E_T$ is corrected for JES, measured muon p_T, electron and τ_h energy scales. The JES corrected $\displaystyle{\not}E_T$ vector is obtained by adding the difference between the vector sums of uncorrected and JES corrected jet momenta to the uncorrected $\displaystyle{\not}E_T$ vector. The muon correction reflects the fact that muons deposit little energy in the calorimeter, and adjusts the $\displaystyle{\not}E_T$ for the p_T of the muon. Finally, electron and τ_h energy corrections are applied to the appropriate calorimeter cells in the $\displaystyle{\not}E_T$ calculation.

IV. MODELING SM PREDICTIONS

A. SM Event Generation

We generally estimate SM processes with MC generated events. A model-independent search incorporates many different processes to properly model the data. We use two generators for this purpose, ALPGEN [16] for generation of all processes, except for diboson production which is generated with PYTHIA [17]. PYTHIA is also used for hadronization and showering.

ALPGEN uses exact matrix elements at leading orders for QCD and electroweak interactions. The benefit of using ALPGEN comes from its ability to calculate exact leading order terms for processes that include high jet multiplicities. ALPGEN produces parton-level events with information on color and flavor, and can be matched to PYTHIA for parton evolution and hadronization.

Matching of a parton from ALPGEN to PYTHIA showering has the fundamental difficulty of separation of the hard interaction from initial-state radiation (ISR) and final-state radiation (FSR). To address this problem we use the MLM matching scheme [18]. In this scheme each final state parton from the matrix element is matched in $\Delta\mathcal{R}$ to an evolved jet. We further reject events which contain an additional jet not matched to a final state parton, except in the sample with the highest number of final state partons.

The following processes are considered, where j is a light jet (g,u,d, or s), ℓ is a lepton, N is an integer ≥ 0 and lp represents a light parton:

1. $W + Nj$
2. $Z/\gamma^* + Nj$
3. $W + c\bar{c} + Nj$
4. $W + b\bar{b} + Nj$
5. $Z/\gamma^* + c\bar{c} + Nj$
6. $Z/\gamma^* + b\bar{b} + Nj$
7. $t\bar{t} \to (2\ell + 2\nu + 2b) + Nj$
8. $t\bar{t} \to (\ell\nu + 2b + 2lp) + Nj$
9. WW
10. WZ
11. ZZ

Since this analysis does not include events with identified photons, we do not consider the contributions to the background from the $W\gamma$ and $Z\gamma$ processes. The processes involving heavy flavor (HF) quarks (c and b) are treated separately from light quark processes because they are often associated with particularly interesting final states, and we generate large number of MC events for these final states. Some of these processes are included in the light parton simulations, so we remove the events with heavy flavor quarks from the light-parton samples so as to avoid double-counting.

For some objects, other programs provide more accurate simulations of their properties and decays. Specifically, TAUOLA [19] is used for τ decays, and EVTGEN [20] is used for the decay of b hadrons. Where needed, correction factors for the cross sections, corresponding to contributions from higher order diagrams, are determined through the normalization procedure based on the inclusive final states as discussed in Sec. V.

We assume a mass of 172.5 GeV for the top quark, consistent with recent measurements [21].

B. Detector Simulation

The events produced from the above combination of generators are processed through the D0 detector simulation and combined with random beam crossing events taken from data (Sec. IV B 1). The detector simulation is based on GEANT 3.2.1 [22], to which two types of correction factors are applied. The first type of correction is event reweighting, where an overall correction is applied to the MC event, rather than to the measured kinematic properties of reconstructed objects. For example, we apply weights to account for the difference in reconstruction efficiencies between data and MC. Another type of correction modifies the objects in a MC event to account for the fact that the simulation has better resolution and a different energy scale than the detector. These corrections generally depend on properties of the objects in an

event. The specific corrections used in this analysis are described below.

1. Instantaneous Luminosity Reweighting

As the instantaneous luminosity profiles of the random beam crossing events and the data are not identical , the MC is reweighted to match the instantaneous luminosity distribution in data. During the course of the data taking period corresponding to the data used for this search the number of average collisions per beam crossing increased from 2 to 6.

2. z_{PV} Reweighting

Our simulated events have a narrower z_{PV} distribution than is observed in data. We therefore apply a weight to each event, based on the z_{PV} of the event, to increase the relative weight of events farther from the center of our detector to match the observed distribution.

3. JES

We apply JES corrections to jets in both data and MC [23]. The purpose of the JES corrections is to correct the measured jet energy to that of the particles in the jet. Jet energies initially determined from the calorimeter cell energies do not exactly correspond to the energies of final state particles that traverse the calorimeter. As a result, a detailed calibration is applied separately in data and MC. In general, the energy of all final state particles inside the jet cone, E_j^{ptcl}, can be related to the energy measured inside the jet cone, E_j, by $E_j^{\mathrm{ptcl}} = (E_j - O)/(R\,S)$. Here, O denotes an offset energy, primarily from additional interactions in or out of time with an event. R is the average response of the calorimeter to the particles in a jet, and S is the correction factor for the net energy loss from particles that scatter out of or into the jet cone. For a given cone radius, O and S are functions of the jet η within the detector. O is also a function of the number of reconstructed event vertices and the instantaneous luminosity; R is the largest correction factor and reflects the lower response of the calorimeter to charged hadrons relative to electrons and photons. It also includes the effect of particle energy loss in front of the calorimeter. The primary response correction is derived from studies of γ+jet events, and depends on jet energy and pseudorapidity. For all jets that contain non-isolated muons, we add the muon momenta to that of the jet. Under the assumption that these muons are from semileptonic decays of b quarks, we also add an estimated average neutrino momentum assumed to be collinear with the jet direction.

4. Jet Shifting, Smearing, and Removal (JSSR)

Additional corrections beyond the JES are needed to take into account threshold and resolution effects for jets. The JSSR corrections are determined from $Z/\gamma \to ee$ + 1 jet events. The Z/γ and the jet should be produced approximately back-to-back in ϕ with the same p_T. This is quantified by a p_T imbalance variable, $\Delta S = \left(p_T^j - p_T^{Z/\gamma}\right)/p_T^{Z/\gamma}$. For jets with a p_T well above the reconstruction threshold, the distribution of ΔS is Gaussian in both data and MC. The difference in the means of these distributions yields a shift that is applied to the MC jet energies to match the data, and a smearing is applied to MC jets based on the difference in the standard deviations of these distributions. Jets that fail the $p_T > 20$ GeV requirement after shifting and smearing corrections are removed from further consideration.

5. Efficiencies

The efficiency of the MC simulation of our detector tends to be larger than the true efficiency of the detector. To account for this, we introduce scale factors to adjust the MC efficiency to match that observed in data. The efficiencies for electrons and muons are obtained using $Z \to ee$ and $Z \to \mu\mu$ events. One of the decay products of the Z boson is the tag object, which is required to pass restrictive reconstruction requirements and be matched to an object that could have fired the trigger for the event. Object efficiencies are then obtained using the second object from the Z decay.

6. Track P_T Resolution

Electron energies are measured in the calorimeter. However, energy deposition does not depend on the charge of the electron, which is determined by the curvature of the associated track in the magnetic field. An incorrectly reconstructed track can therefore lead to an incorrect charge assignment. Bremsstrahlung from electrons can affect the curvature of the tracks. Also, a soft interaction in the inner detector can result in the process $e^+ \to e^+ e^- e^+$, leading to charge misidentification if the wrong sign electron track is associated with the electron. This difficulty is also present in tau decays when at least one hadron is produced.

Because the rate of charge misidentification is not properly modeled in the detector simulation, we add a scale factor to electron and tau MC events to approximate the appropriate rate of charge mis-identification. We determine this scale factor by using dielectron events consistent with $Z \to ee$ decays; and we only consider events with dielectron invariant mass between 70 to 110 GeV to avoid biases against physics beyond the SM. The charge misidentification rate in data is about 1%, while

the MC predicts a rate of 0.5%.

The disagreement in track resolution between the data and MC also affects muon p_T measurement, which is corrected using smearing parameters determined by comparing the data and MC mass peaks for $Z \to \mu\mu$ and $J/\psi \to \mu\mu$ decays.

7. Electron Energy Smearing

In the simulation, the electron p_T reconstructed in the calorimeter has a better resolution than in the data. We correct this using a Gaussian smearing function tuned to reproduce the shape of the $Z \to ee$ peak.

8. Jet Taggability

The jet taggability rates (Sec. III F) are found to be different for MC and data. To correct for this difference, correction factors are applied as scale factors depending on p_T, η and z_{PV} of the jet [24].

9. b-tagging Rate

As detailed in Sec. III F, we apply a tagging algorithm to both data and MC jets to select jets originating from heavy (b/c) quarks. However, the algorithm can select mistagged light jets. The tagging rates (for both heavy and light parton jets) depend on the p_T and η of the jets. The heavy-quark tagging rates are measured separately in both data and MC using dedicated samples. The performance of the b-tagging algorithm in MC events is better than in data. To correct the tagging rates in MC events, we first determine the flavor of the tagged jet by matching it in $\Delta\mathcal{R}$ with the initial parton. Depending on the flavor of the jet, we apply a per-jet scale factor given by $\mathrm{SF} = \epsilon^{data}(p_T, \eta)/\epsilon^{MC}(p_T, \eta)$, where $\epsilon^{\mathrm{data}}(p_T, \eta)$ and $\epsilon^{MC}(p_T, \eta)$ are the b-tagging efficiencies for a given parton flavor for data (MC) events. To maintain correct normalization, a small downward correction is applied to non-b-tagged jets.

10. Weak Gauge Boson p_T

The p_T distribution of the Z boson from ALPGEN MC is corrected to match the distribution observed in data in $Z \to ee$ decays [25]. A modified reweighting is carried over to the W boson p_T based on the theoretical ratio of the W to Z p_T spectra [26].

11. $\Delta\phi$

We apply a $\Delta\phi$-dependent weight derived specifically for this analysis using the inclusive distributions de-scribed in Sec. V to correct the $\Delta\phi$ between leptons in dilepton final states and the lepton and $\not{E}_T$ in single-lepton + jets final states. This additional correction is required because the limited detector resolution at small p_T values prevents us from obtaining a good description of the $\Delta\phi$ distribution in the region $p_T \approx 0$, which is dominated by SM processes, by using only the correction on the weak boson p_T [27]. We remove events containing high p_T objects, using the same method described in Sec. VI, from the fit to avoid introducing biases from possible new physics signals. This reweighting affects not only the $\Delta\phi$ distributions, but also other quantities that depend on the angular distribution of particles such as the p_T of the W boson.

V. INCLUSIVE FINAL STATES

To determine the unknown scale factors from the data, we construct seven inclusive final states each dominated by a specific SM process. These seven inclusive non-overlapping final states are specified in Table I by the relevant objects and their selection criteria. The additional objects (X in the table) are selected as shown in Table II. We reject events that include a photon in the CC with a $p_T > 15$ GeV, mainly due to difficulties in modeling. Events with real photon misidentified as electrons could contaminate the e+jets, and the dilepton or trilepton final states containing at least one electrons. We have estimated the contributions from such backgrounds and consider them negligible in the region of the phase space that is relevant for the search for physics beyond the SM. The seven states ($e + $ jets, $\mu + $ jets, ee, $\mu\mu$, μe, $e\tau$, $\mu\tau$) were each selected to correspond to a specific SM process.

- $e + $ jets

  The electron + jets final states have more background from multijet events, where a jet is misidentified as an electron, than the other electron final states. Therefore the likelihood criterion used is tighter than in other final states, $\mathcal{L}_e > 0.95$. We also require at least one jet having $E_T > 20$ GeV, $\not{E}_T > 20$ GeV, and an e $p_T > 35$ GeV. This final state is dominated by $W + $ jets events with $W \to e\nu$ decays. The multijet background in this final state is estimated using a sample of events with exactly one non-isolated electron with a $p_T > 35$ GeV and the same jet and $\not{E}_T$ criteria as in signal.

- $\mu + $ jets

  The $\mu + $ jets final state is dominated by $W + $ jets events with $W \to \mu\nu$ decays. To reduce the amount of multijet background, at least one jet having $E_T > 20$ GeV is required, as well as $\not{E}_T > 20$ GeV and a muon with $p_T > 25$ GeV. Just as the $e + $ jets final state, this final state is inclusive in jets with no other additional objects allowed. The

TABLE I: Inclusive final states and their object selections, where $p_T^{\min}$ is the minimum allowed value of p_T and $|\eta|^{\max}$ is the maximum allowed value of $|\eta|$.

Final State	Object	$p_T^{\min}$ (GeV)	$|\eta|^{\max}$
e + jets + X^a	e	35	1.1
	jet	20	2.5
	$\not{E}_T$	20	-
μ + jets + X^b	μ	25	1.5
	jet	20	2.5
	$\not{E}_T$	20	-
$ee + X^c$	e	20	1.1
$\mu\mu + X^d$	μ	15	1.5
$\mu e + X^e$	μ	15	1.5
	e	15	1.1
$e\tau + X^f$	e	15	1.1
	τ	15	1.1
$\mu\tau + X^g$	μ	15	1.5
	τ	15	1.1

^{a} $X \neq e, \mu, \tau, \gamma$
^{b} $X \neq e, \mu, \tau, \gamma$
^{c} $X \neq \mu, \tau, \gamma$
^{d} $X \neq e, \tau, \gamma$
^{e} $X \neq \tau, \gamma$
^{f} $X \neq \gamma$
^{g} $X \neq e, \gamma$

TABLE II: Criteria required for inclusion as additional objects (X) in one of the seven final states listed in Table I.

Object	$p_T^{\min}$ (GeV)	$|\eta|^{\max}$
e	15	1.1
μ	15	1.5
τ	15	1.1
jet	20	2.5

multijet background in this final state is estimated using a sample of non-isolated muons with $p_T > 25$ GeV and the same jet and $\not{E}_T$ requirements as isolated muons.

- ee

  The dielectron final state requires each electron to have $p_T > 20$ GeV and $\mathcal{L}_e > 0.85$. The electrons are also restricted to be in the central calorimeter, $|\eta| < 1.1$, and the jets have the same criteria as for the other final states. This final state is dominated by $Z/\gamma^* \to ee$ events. No multijet background is necessary in this channel to produce a satisfactory normalization fit.

- $\mu\mu$

  The dimuon final state requires at least two muons with the muon-p_T criteria lowered to $p_T > 15$ GeV because of the smaller contribution from multijet background. Any jet must have $p_T > 20$ GeV. This

final state is inclusive in both jets and muons, but an additional e or τ lepton places the event in the μe or $\mu\tau$ final states. Analogous to the ee channel, this final state is dominated by $Z/\gamma^* \to \mu\mu$ events. No multijet background is necessary in this channel to produce a satisfactory normalization fit.

- μe

  The μe final state is inclusive except for τ leptons; $e\mu\tau$ events are assigned to the $e\tau$ final state. This final state is dominated by $Z/\gamma^* \to \tau\tau$ events. The multijet background in this final state is estimated from a sample consisting of non-isolated electrons and isolated muons, and contains both multijet and W + jet events.

- $e\tau$

  The $e\tau$ sample is inclusive in all objects. The electron and τ_h p_T are required to be at least 15 GeV. The electron likelihood is set to $L_e > 0.95$ to reduce the large multijet background as many apparent τ_h correspond to misidentified jets. The parameter that separates electron from hadronic taus, NN_e, is set to 0.8 to reduce the contribution from dielectron events. This final state is also dominated by $Z/\gamma^* \to \tau\tau$ events. The multijet background in this final state is estimated from a sample of isolated electrons and non-isolated τ leptons, and contains both multijet and W + jet events.

- $\mu\tau$

  The $\mu\tau$ state contains at least one muon and one τ_h. It is inclusive in all objects except electrons, whose presence would move the event to the $e\tau$ final state. This final state is also dominated by $Z/\gamma^* \to \tau\tau$ events. The multijet background in this final state is estimated from a sample of isolated muons and non-isolated τ leptons, and contains both multijet and W + jet events.

VI. INCLUSIVE NORMALIZATION FITS

Our model does not provide proper normalization of different MC contributions because, for example, of higher-order corrections needed for the leading-order or leading-logarithm cross section calculations. To avoid uncertainties in normalization, we perform a fit, described below, for each of the inclusive final states to obtain scale factors that reproduce the distributions of the selected data using a combination of the SM MC and multijet predictions determined from data. We treat the Drell-Yan (D-Y) contributions to the ee and $\mu\mu$ final states without light partons separately from those with light partons because it improves agreement between data and MC.

The fits for normalization factors are performed on kinematic distributions of different object quantities, altering the overall normalization of each input process

contributing to the final state so that the χ^2 probability for that final state is minimized for the combined fit. To avoid fitting to data at the highest values of p_T, where new physical processes can be important, we only use events that are not in the high p_T tail, which is defined as containing 10% of the events. Distributions of basic quantities such as $\not{E}_T$, p_T, η, $\Delta\phi(\text{obj}, \not{E}_T)$ of leptons and jets (here obj refers to the momentum vector of the object considered) are used in the fits while more complex variables are used to check the quality of the overall fit. The latter variables include the mass or transverse mass $M_T = \sqrt{(p_{T,1} + p_{T,2})^2 - (\vec{p}_{T,1} + \vec{p}_{T,2})^2}$ of two or more objects, jet multiplicities, and the p_T of the W and Z bosons. If an event contains any object outside the p_T range defined above, then none of the objects in the event are used in the fit.

The list of the seven final states, the processes that are normalized through the inclusive fits to each of the final states, and the number of events in each final state are shown in Table III. Once the fitted values are extracted, the distributions are rescaled accordingly, and the total background contribution, B, for a particular final state is

$$B = \sum_i^{N_{bkg}} S_i B_i \qquad (1)$$

where the scale factor (S_i) for each background process (B_i) is determined from the final state in which its contribution is most important and that scale factor is used in all other final states to which that background contributes. N_{bkg} refers the total number of all the SM processes contributing to a particular final state.

A simplified example for the $e + \text{jets} + X$ final state ($X \neq e, \mu, \tau, \gamma$) is used to illustrate the procedure. The $e + \text{jets} + X$ state is dominated by $W \to e\nu$ events, but there is a significant contribution from multijet and Drell-Yan events. We use the normalization factor for the Drell-Yan process, determined through a separate fit to the $ee + X$ final state ($X \neq \mu, \tau, \gamma$), in the $e + \text{jets}$ fit. We also fix the scale factors to one for rare processes which have contributions that are too small to fit accurately in $e + \text{jets}$, such as the $t\bar{t}$ contribution. We then fit for the SM W boson and multijet contributions in the data. The fit optimizes agreement between the distributions in data and the SM prediction for the variables listed above. The result of the fit is two overall weights, one for $W \to e\nu$ and one for multijet $\to e + \text{jets}$.

In the ee and $\mu\mu$ final states, there are three contributions allowed to float relative to each other, $Z + 0\text{lp}$, $Z + 1\text{-}3$ lp, and the number of $W/Z + \text{hf}$ events. In the $e + \text{jets}$ and $\mu + \text{jets}$, the Z contribution is held fixed to the values found in the ee and $\mu\mu$ fits, and the $W + \text{lp}$, multijet, and $W + \text{hf}$ contributions are allowed to float. In the $\mu\tau$, and μe final states, the multijet and $Z \to \tau\tau$ contributions are allowed to float, while other Z contributions are fixed to values given by the fits to the ee and $\mu\mu$ final states. The $e\tau$ final state is similar,

but the $Z \to ee$ contribution is large enough that we also allow the normalization of this contribution to float.In all final states, the number of $t\bar{t}$ and diboson events are held fixed to the best available calculations of the cross sections (approximate next-to-next-to-leading order for $t\bar{t}$ and next-to-leading order for WW) [28]. The ratio of $W/Z + b\bar{b}$ to $W/Z + c\bar{c}$ are also held fixed to the expected ratio from next-to-leading order calculations [29].

The distributions of the variables for the input processes are not varied, only their relative contributions. The fit is performed using the MINUIT program [30]. For single-lepton states and hadronic τ final states, multijet events are a significant background. We assume that the contribution from other SM processes modeled by the MC samples to the multijet background is small. The scale factors of input processes for the MC events should also account for the contributions of the processes to the multijet background. The main effects of contributions from any of the MC processes to the multijet background would be to decrease the scale factor for backgrounds modeled by MC.

The main purpose of the normalization process is to assure that the fundamental SM processes are well-modeled. The results of the fit are then checked for qualitative agreement with the data. The overall scale factors are checked to compare to those from dedicated analyses. If the normalization factors are properly included in the MC, then all the scale factors should equal unity. In the $e + \text{jets} + X$ and $\mu + \text{jets} + X$ final states, the scale factors for the $W + \text{light partons}$ are consistent within uncertainties between the electron and muon channels. The small deviation of the scale factors from unity is caused by the presence of small contributions from $W + \text{jet}$ events in which the W decays leptonically in the samples used for the estimation of the multijet backgrounds.

The scale factors needed for the $Z + \text{light parton}$ MC are consistent with 1 for the $Z + 1\text{-}3$ lp MC, but not for the $Z + 0$ lp MC. This difference is due to systematics that we do not account for in this analysis, e.g., uncertainties on the Z p_T reweighting, jet energy scale and lepton ID. The total contribution of $Z \to ee$ to the $e\tau$ final state is within 10% of the expected value from the ee fit. The ratio of the scale factors for the $W/Z + b\bar{b}(c\bar{c})$ MC relative to the $W/Z + \text{lp}$ MC obtained from the fits is consistent, within errors, with the NLO predictions [29].

One histogram that is included in the overall fit and one check histogram that is not part of the fit are shown for each of the seven final states in Figs. 1 – 7. In the figures, the leading and second electron are the electrons with highest p_T in the event and next highest p_T in the event, with a similar definition for leading and second muons and jets.

The electron p_T distribution in Fig. 1 shows a clear disagreement between data and simulation in this kinematic region arising from the need for a large multijet contribution at low p_T, and other variables that provide better agreement with a smaller multijet contribution. However, the discrepancy at low p_T should not mask the

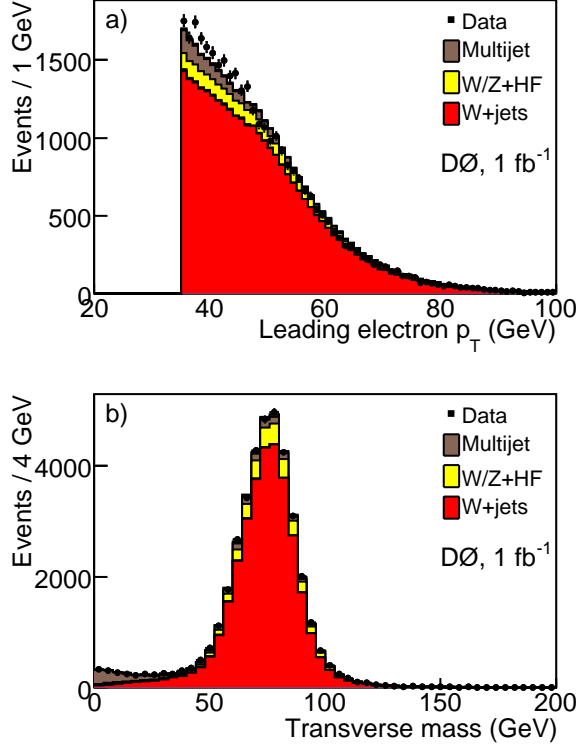presence of new physics at high p_T, which is the main focus of this analysis.

FIG. 1: (color online) e + jets final state (a) electron p_T histogram and (b) transverse mass $(e, \not{E}_T)$ check histogram.

VII. EXCLUSIVE FINAL STATES

After determining the normalization scale factors, the seven inclusive subsets are merged to create an input file for the VISTA algorithm [8]. Each MC and background event is given a weight calculated from the data based scale factors and any required corrections. The VISTA algorithm, developed by the CDF Collaboration, is a tool that performs a broad check of the agreement between data and the SM. We modified the CDF algorithm for our analysis strategy as described above. The resultant VISTA@D0 algorithm focuses on the D0 high p_T data to determine whether the data can be adequately described by the SM or if significant discrepancies can be confirmed. VISTA mainly examines discrepancies that affect the overall distributions rather than narrow regions of phase space, addressing the numbers of expected events and MC/data agreement across full distributions of chosen variables.

The events are separated into homogeneous subsets of events according to the objects contained in each event, resulting in 117 exclusive final states. Examples of such
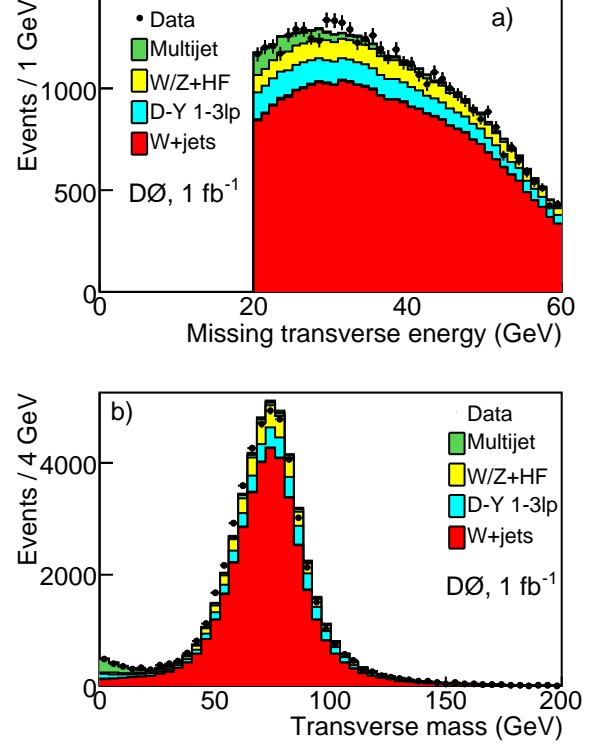

FIG. 2: (color online) μ + jets final state (a) $\not{E}_T$ histogram and (b) transverse mass $(\mu, \not{E}_T)$ check histogram.

TABLE III: The contributions used in the inclusive fits for each of the inclusive final states and the number of selected data events in each. The dominant SM process is listed first for each final state. In the $e\tau$ and $\mu\tau$ final states, the multijet background also includes a contribution from W + jets.

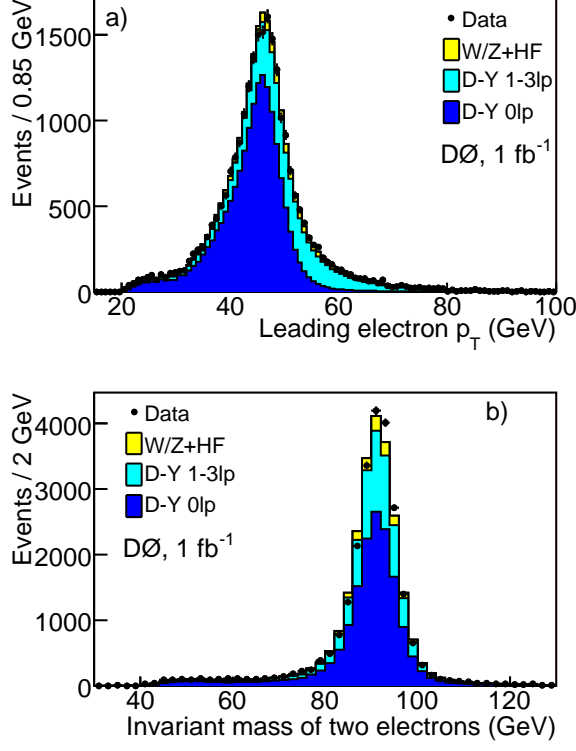| State	SM process	Events
e + jets + X	W + jets	40k
	Multijet	
	W/Z + HF	
μ + jets + X	W + jets	50k
	Multijet	
	W/Z + HF	
ee + X	D-Y + 0lp	25k
	D-Y 1-3lp	
	W/Z + HF	
$\mu\mu$ + X	D-Y + 0 lp	24k
	D-Y + 1-3 lp	
	W/Z + HF	
μe + X	$Z \to \tau\tau$	0.34k
	Multijet	
$e\tau$ + X	$Z \to \tau\tau$	1.3k
	Multijet	
	$Z \to ee$	
$\mu\tau$ + X	$Z \to \tau\tau$	1.0k
	Multijet	

FIG. 3: (color online) ee final state (a) leading electron (with highest p_T) p_T fit histogram and (b) invariant mass (e,e) check histogram.

FIG. 4: (color online) $\mu\mu$ final state (a) leading muon p_T fit histogram and (b) invariant mass (μ,μ) check histogram.

exclusive final states include $\mu^{\pm}\tau^{\mp} + 2$ jets $+ \not{E}_T$, $e^{\pm}\mu^{\mp} + 2$ jets $+ \not{E}_T$, $e^+e^+ + 3$ jets, and $\mu + 4$ jets $+ \not{E}_T$.

VISTA performs two types of checks: first, it does a normalization-only check on the number of events in each exclusive state; the goodness of the fit is calculated using Poisson probabilities. Second, it calculates a Kolmogorov-Smirnov statistic (and resulting fit probability) for the consistency of all the kinematic distributions in any final state with the predicted SM distributions. Both of these results require additional interpretation because of the large number of trials (number of final states and/or the number of distributions) involved. When observing many final states, some disagreement is expected from statistical fluctuations in the data. Thus the Poisson probability used to determine agreement is corrected to reflect this multiple testing. A similar effect occurs when comparing kinematic distributions, and again the probabilities are first converted to standard deviations and then corrected for the number of distributions examined.

Another algorithm we use to search for new physics is called SLEUTH [5], used at D0 for the analysis of the data collected during Run I (1992-1996) of the Tevatron. SLEUTH is an attempt to systematically search for new physics as an excess at the largest values of $\sum p_T$. This variable corresponds to the sum of the values of
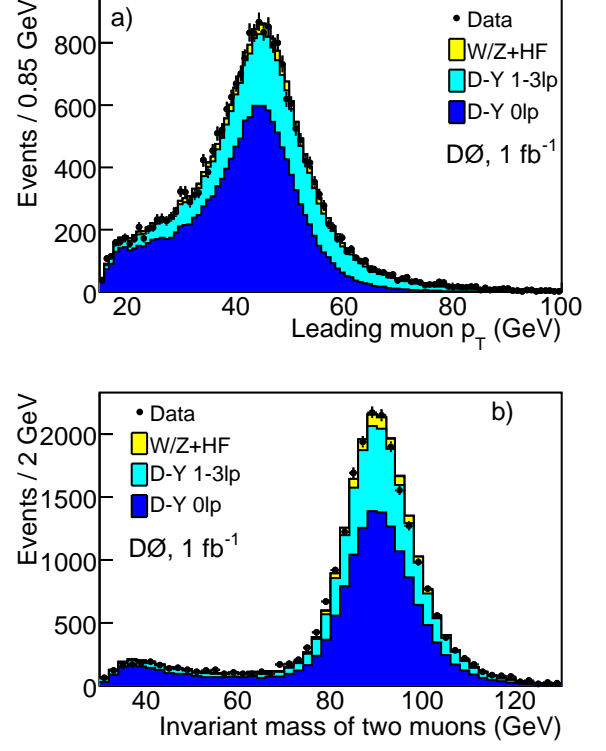
the scalar p_T of all objects in the event, including the $\not{E}_T$. The SLEUTH algorithm is quasi-model independent, where "quasi" refers to the assumption that the physics beyond the SM will appear as an excess of events in some final state at large $\sum p_T$.

For SLEUTH, the VISTA exclusive X + 0 jet and X + 1 jet final states are merged, as are the X + 2 jets and X + 3 jets final states, and light-lepton universality is assumed, combining eX and μX channels. Underlying these assumptions is the belief that any new physics will leave similar signatures in events with no radiative jets or one radiative jet, and in electron and muon final states. Therefore combining these final states increases the statistics in each final state while reducing the trials factor needed to account for looking in multiple final states. In each final state, the $\sum p_T$ distribution is scanned to find the cutoff above which the significance of any excess in data relative to the SM background is maximal, with the condition that at least three events be observed above the cutoff. This defines the most interesting region for this final state. Next, pseudo-experiments are generated with pseudo data pulled from the SM background expectation for this final state, and the fraction of pseudo-experiments is determined in which the most interesting region is at least as interesting as the most interesting region found in real data. This gives the probability that the most significant excess observed in the
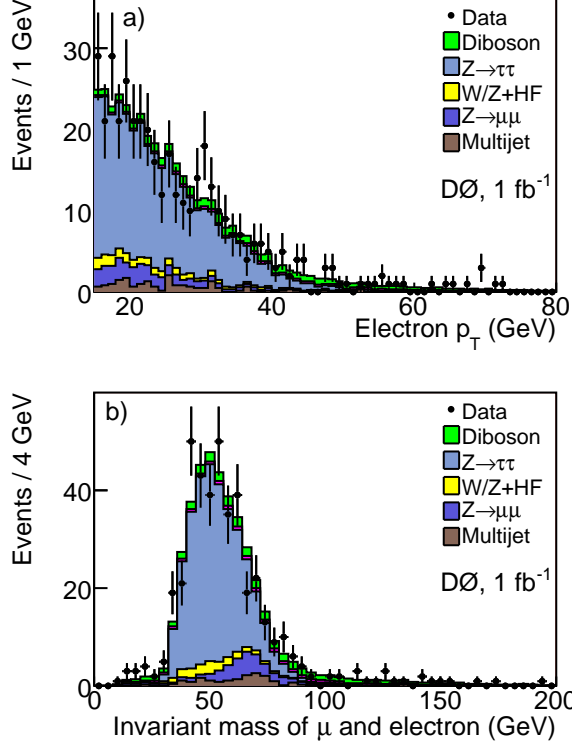
FIG. 5: (color online) μe final state (a) electron p_T fit histogram and (b) invariant mass (μ, e) check histogram.

FIG. 6: (color online) $e\tau$ final state (a) The $\Delta\phi(e, \not{E}_T)$ fit histogram and (b) invariant mass (e, τ) check histogram.

considered final state arise from a background fluctuation. Finally, a corrected probability is estimated from the fraction of hypothetical experiments that would produce a region in any final state at least as interesting as the most interesting region observed among all final states in real data. We define a significant output from SLEUTH as one with a corrected probability of < 0.001 (that is over 3 Gaussian standard deviations from the SM prediction using a one-sided confidence interval).

VIII. SENSITIVITY TEST

To check the sensitivity of a search with SLEUTH, we examine whether a top quark (produced in $t\bar{t}$ pairs) which contributes objects with high p_T would have been discovered in the current data sample. For this test, we used all the background samples, except for the $t\bar{t}$ MC. The main concern is whether other final states would compensate for the missing $t\bar{t}$ events, and thus SLEUTH would not be sensitive to $t\bar{t}$ production in data.

We examine the $\ell jjb\bar{b}\not{E}_T$ final state, which we expect to be dominated by $t\bar{t}$ events. Figure 8 shows that presence or absence of a $t\bar{t}$ signal has a great impact. With a threshold of 0.001, the SLEUTH test, including the $t\bar{t}$ MC, yields a statistical probability of compatibility of 0.98 after correcting for the number of trials. However, without
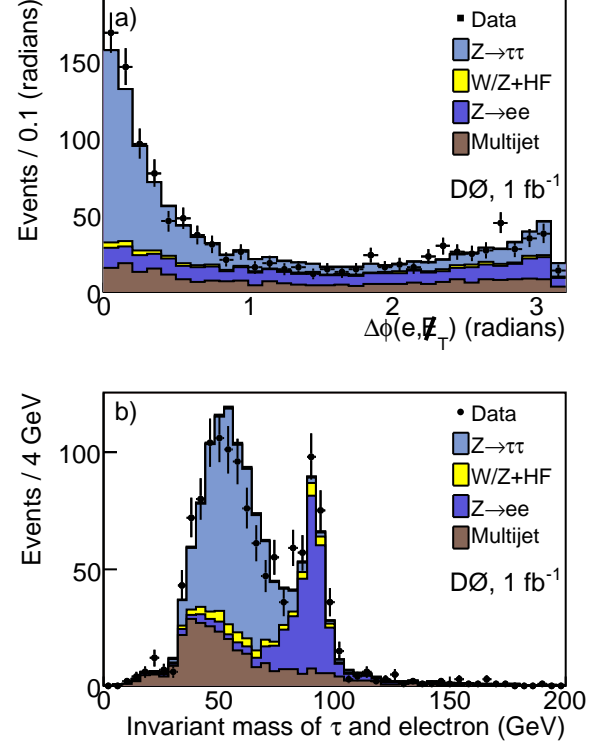
the $t\bar{t}$ contribution this probability is $< 1.1 \times 10^{-5}$. In Fig. 8 and other SLEUTH plots, the insets show the results for data and MC that pass the $\sum p_T$ cut maximizing the significance of excess in data.

IX. RESULTS

A. Numerical discrepancy using the VISTA analysis

In VISTA, the separation of the input data into final states completely defined by the objects in an event, yields a total of 117 unique exclusive final states. The probability $(\tilde{\mathcal{P}})$ that the yield observed in data results from a statistical fluctuation of the SM sample in channel f_s is determined from

$$\tilde{\mathcal{P}} = 1 - (1 - p_{fs})^{N_{fs}} \overset{p_{fs} \ll 1}{\approx} N_{fs} \times p_{fs} \qquad (2)$$

where N_{fs} is the number of trials and p_{fs} is the probability that the number of events predicted for the channel f_s in the SM would fluctuate to what is observed in data, before applying the correction for the number of trials. The number of trials is $N_{fs} = 117$, corresponding to the
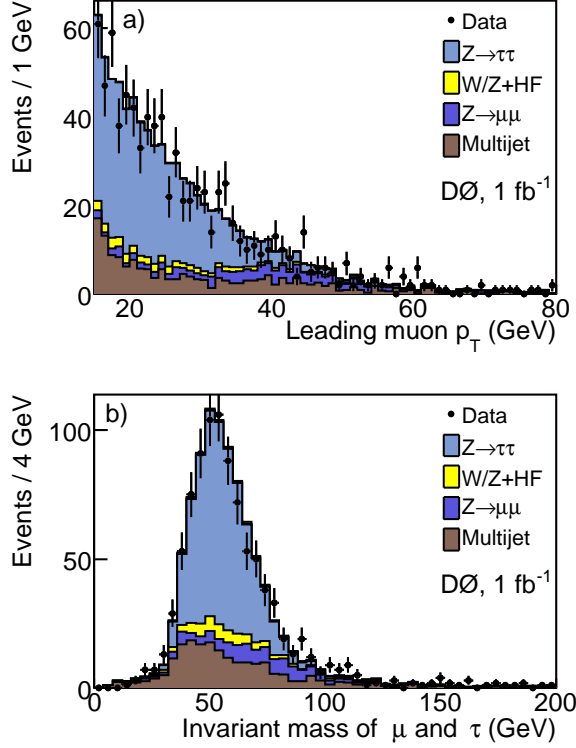
FIG. 7: (color online) $\mu\tau$ final state (a) muon p_T fit histogram and (b) invariant mass (μ, τ) check histogram.

number of final states, and

$$p_{fs} = \int_0^\infty \exp\left[-\frac{(N-N_B)^2}{2\sigma_B^2}\right] dN \sum_{N_{\text{data}}}^\infty \frac{N^i}{i!} e^{-N}, \quad (3)$$

where N_B and σ_B are the expected SM event yield from background and its uncertainty, respectively, and N_{data} is the number of events observed in any channel. The Gaussian significance is the value of σ that satisfies the equation

$$\int_\sigma^\infty \frac{1}{\sqrt{2\pi}} e^{-\frac{x^2}{2}} dx = \tilde{\mathcal{P}}. \quad (4)$$

The final state probabilities converted into standard deviations, before the correction factor for the number of trials, are shown in Fig. 9. This distribution shows most final states near $\sigma = 0$, with some excess for $\sigma > 3$. Of the 117 final states, two show significant discrepancy after correction for the number of trials. These are the final states $\mu + 2$ jets $+ \not{E}_T$, with a probability corresponding to a 4.5 σ discrepancy, and $\mu^+\mu^- + \not{E}_T$ with a discrepancy of 6.7σ (also shown in Fig 9).

The discrepancy for the $\mu + 2$ jets $+ \not{E}_T$ final state shows the greatest difference from the SM prediction in the modeling of jet distributions. There is a significant excess in the number of jets at high $|\eta|$, which points to
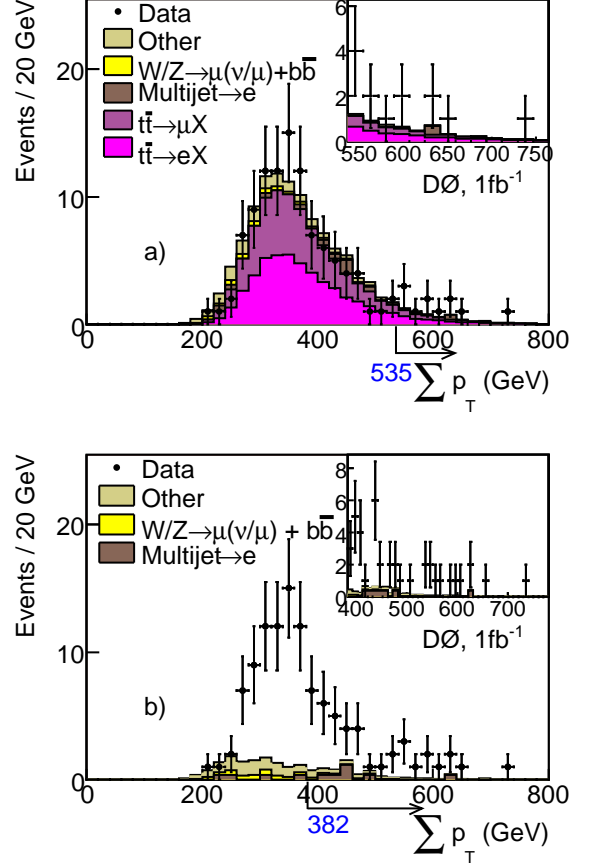

FIG. 8: (color online) Sensitivity to new physics test using the $t\bar{t}$ final state. (a) The $t\bar{t}$ MC is included, yielding only minor differences between data and SM background. The statistical agreement between the data and MC for the distribution shown on inset is nearly 2 σ. (b) The results of the entire analysis without the $t\bar{t}$ MC. In this case, SLEUTH passes the criterion of interest at 0.001 for this final state. The insets show the distribution beyond the $\sum p_T$ cutoff. "Other" refers to contributions too small to list, including $W + b\bar{b} \to e\nu b\bar{b}$ events, $W + c\bar{c} \to \ell\nu c\bar{c}$ events, $W + lp \to \ell\nu + lp$ events, and diboson events.

likely problems with modeling ISR/FSR jets in the forward region, as can be seen in Fig. 10a. This difference is observed in dedicated analyses [31], and the discrepancy becomes less severe when using SHERPA [32] MC events.

The $\mu^+\mu^- + \not{E}_T$ discrepancy can be attributed to difficulties modeling the muon momentum distribution for high p_T muons. As noted in Sec. IV B 6, the muon smearing modeling is based on muons from Z and J/ψ decays, dominated by muons below 60 GeV, and is not as reliable at high p_T. The prime signature of poorly simulated high p_T muons is an excess of $\not{E}_T$ because of the mismodeling of the resolution of the mismeasured track. The $\Delta\phi$ between the positive muon and $\not{E}_T$ in the $\mu^+\mu^- + \not{E}_T$ final state is shown in Fig. 10b, where the excess tends to be

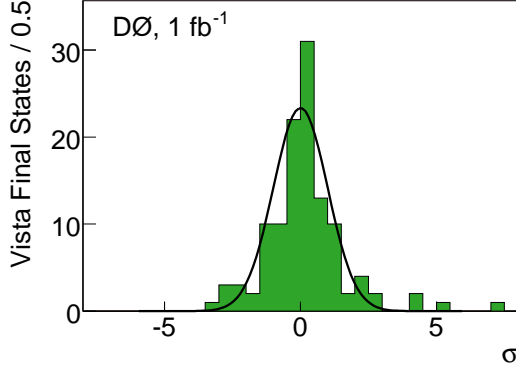for events where the $\not{E}_T$ is collinear with a muon.

FIG. 9: (color online) Distribution of discrepancies for the 117 final states relative to the SM in terms of standard deviations calculated in VISTA final state before accounting for the trials factors. The curve represents a Gaussian distribution centered at zero to guide the eye. The distribution is expected to obey Poisson statistics, which is the reason the distribution is narrower than the Gaussian.

B. VISTA Shape Analysis of Discrepancies in Distributions

The 117 final states contribute a total of 5543 individual one-dimensional distributions in various variables, and comparison between simulation and data is performed for each. The trials-factor adjusted probability is determined from $\tilde{\mathcal{P}} = 1 - (1 - p_{\mathrm{shp}})^{5543}$, where p_{shp} is the Kolmogorov-Smirnov (KS) probability to observe a discrepancy for any individual distribution (before applying the correction for 5543 trials). As with the probability for a final state normalization discrepancy in any final state, the probability for a discrepancy in a spectrum is converted into units of standard deviation. Any deviation $>3\sigma$ is considered discrepant. The distribution of deviations before correction for the number of trials is shown in Fig. 11.

Sixteen distributions are found to be discrepant at the 3σ level after correcting for the trials. The majority of these are related to spatial distributions involving jets. All these discrepancies are related to known simplifications in our modeling assumptions, e.g., no systematic uncertainties taken into account, aside from the adjustments made by the normalization factors. These discrepancies would not be expected to severely affect the SLEUTH search for new physics at high p_T tails. All 16 discrepant distributions are shown in Figs. 12–15 and are listed in Table IV. In the figures, the second jet refers to the lower p_T jet in the two jet final states.
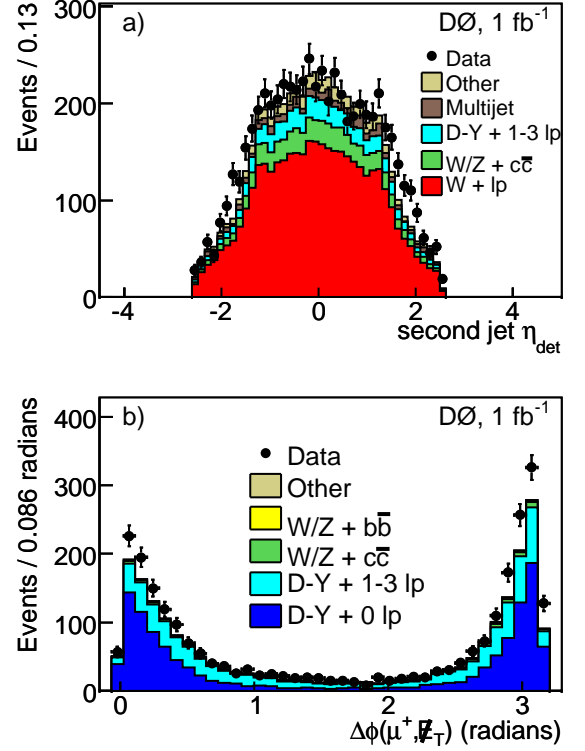

FIG. 10: (color online) (a) The distribution of the pseudorapidity of the second jet with respect to the center of the D0 detector in the $\mu + 2$ jets $+ \not{E}_T$ channel. "Other" contains distributions too small to list individually, $W + b\bar{b}$, diboson, $t\bar{t}$, and D-Y $+ 0$ lp. (b) The $\Delta\phi$ distribution between the μ^+ and the $\not{E}_T$ for the $\mu^+\mu^- + \not{E}_T$ final state. "Other" contains distributions too small to list individually, diboson and $t\bar{t}$.
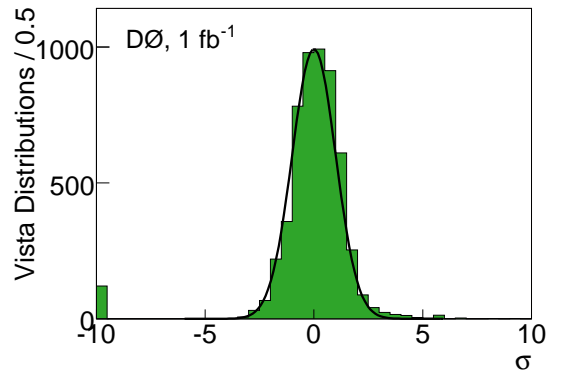

FIG. 11: (color online) The σ distribution for the 5543 VISTA comparisons before accounting for number of the trials. The curve represents a Gaussian distribution centered at zero to guide the eye. There are 116 distributions in the underflow bin with $\sigma \leq -10$. This is expected as histograms with KS probabilities > 0.99999 are rounded to 1, and appear in the underflow bin.
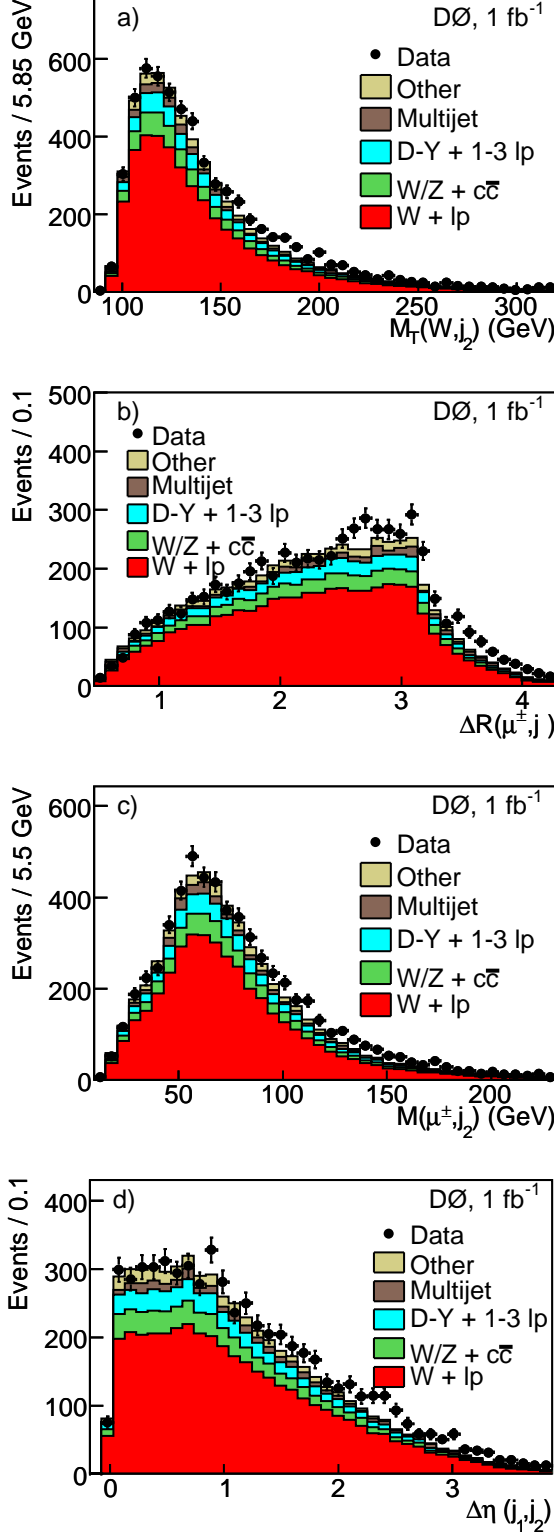
FIG. 12: (color online) The discrepant distributions in the μ + 2 jets + $\not{E}_T$ exclusive final state. (a) The transverse mass distribution of the W boson plus second jet, (b) the $\Delta\mathcal{R}$ between the muon and the second jet, (c) the invariant mass distribution of the μ + second jet, and (d) $\Delta\eta$ between the highest p_T jet and the second jet. "Other" contains distributions too small to list individually, $W + b\bar{b}$, diboson, $t\bar{t}$, and D-Y + 0 lp.

TABLE IV: The full list of VISTA results with discrepant distributions listed by final state.

VISTA Final State	Kinematic Variable	σ
$\mu^\pm$ + 2 jets + $\not{E}_T$	$M_T(W,j_2)$	4.4
	$\Delta\mathcal{R}(\mu, j_2)$	4.4
	$M(\mu,j_2)$	4.0
	$\Delta\eta(j_1, j_2)$	3.8
$\mu^\pm$ + 1 jet + $\not{E}_T$	$p_T(W)$	8.1
	Σp_T	5.1
	$p_T(\mu)$	4.1
	$M_T(\mu^\pm, \not{E}_T)$	4.1
	$\Delta\phi(\mu, j)$	3.1
$e^\pm$ + 2 jets + $\not{E}_T$	$\Delta\eta(j_1, j_2)$	4.2
	$M_T(j_2, \not{E}_T)$	4.0
	$M_T(W,j_2)$	3.0
$e^\pm$ + 1 jet + $\not{E}_T$	$\Delta\phi(e^+, j)$	5.5
	$p_T(e^\pm)$	4.4
	$p_T(W)$	3.8
	$\not{E}_T$	3.1

C. SLEUTH

All VISTA final states are used as input to SLEUTH, and the 117 inclusive final states are folded into 31 final states after applying global charge conjugation invariance, re-binning in the number of jets, and assuming light lepton universality. The two VISTA final states that show broad numerical excesses are found again with the SLEUTH algorithm, as expected. No additional final states have a significant SLEUTH output, as defined in Sec. VII.

In the SLEUTH runs performed at CDF, using a slightly different analysis strategy, the four most interesting observed final states were $\mu^\pm e^\pm$, $\mu^\pm e^\pm$ + 2 jets + $\not{E}_T$, $\mu^\pm e^\pm$ + $\not{E}_T$, and $\ell^\pm \ell^\mp \ell'$ + $\not{E}_T$ in 2.0 fb^{-1} [9] of integrated luminosity. These states were also among the most discrepant observed by CDF in 0.9 fb^{-1} [8] of integrated luminosity. Our results for these states are shown in Figs. 16, 17, and 18, except for $\mu^\pm e^\pm$ + 2 jets + $\not{E}_T$, for which we find no events with 0.16 events expected. Figure 19 shows a related final state, where the muon and electron are of opposite sign rather than of the same sign where CDF sees a discrepancy. None of these states are significantly discrepant in our analysis.

The SLEUTH final states with $\tilde{\mathcal{P}} \leq 0.99$ are shown in Table V. A plot including all of the final state probabilities converted to units of σ can be seen in Fig. 20. The final state $\ell^\pm + \tau^\mp + \not{E}_T$, which was not identified as having a significant discrepancy between data and the SM in VISTA, falls close to our SLEUTH threshold. Figure 21 shows the $\sum p_T$ distribution for this final state.

X. CONCLUSIONS

We have performed a global study of D0 high p_T data to search for significant deviations from the standard
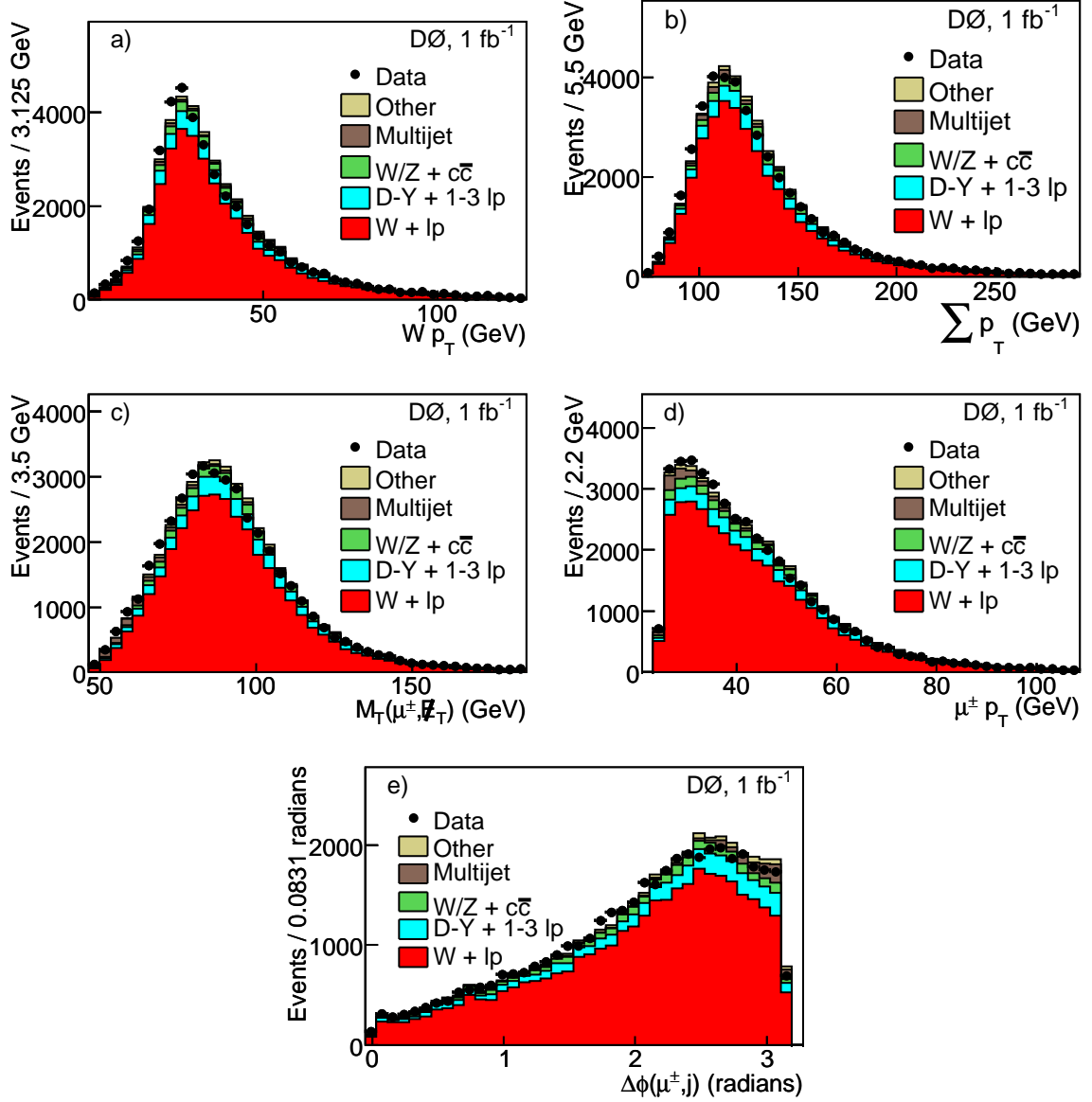
FIG. 13: (color online) The discrepant distributions in the $\mu + 1$ jet $+ \not{E}_T$ exclusive final state: (a) the p_T of the W boson, (b) the sum of the scalar values of p_T of the μ, jet, and $\not{E}_T$, (c) the transverse mass of the μ and $\not{E}_T$, (d) the p_T of the μ, and (e) the $\Delta\phi$ between the muon and the jet. "Other" contains distributions too small to list individually, $W + b\bar{b}$, diboson, $t\bar{t}$, and D-Y $+ 0$ lp.

model. This broad search for BSM physics is based on 1.1 fb^{-1} of integrated luminosity collected in Run II of the Fermilab Tevatron Collider in the D0 experiment. Using the VISTA algorithm, a total of 117 exclusive final states and 5543 kinematic distributions were compared to the SM background predictions. Only two out of 117 exclusive final states, $\mu^{\pm} + 2$ jets $+ \not{E}_T$ and $\mu^+\mu^- + \not{E}_T$, show a statistically significant discrepancy. Given the known modeling difficulties in both final states together with our neglect in this study of systematical uncertainties, we cannot attribute the observed discrepancies to

sources of physics beyond the standard model. A quasi-model-independent search for new physics was also performed using the algorithm SLEUTH by looking for statistically significant excess at high $\sum p_T$ in a wide array of exclusive final states. No additional final states cross the discovery threshold in SLEUTH beyond the excesses noted by VISTA.
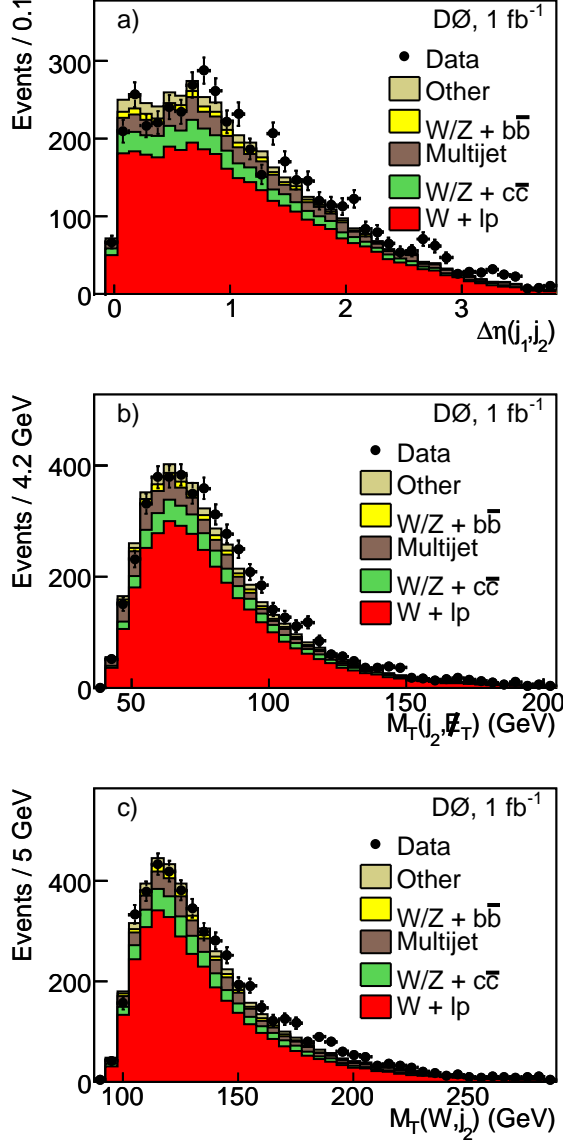
FIG. 14: (color online) The discrepant histograms in the $e + 2$ jets $+ \rlap{E}{/}_T$ exclusive final state. (a) The $\Delta\eta$ between the two jets, (b) the transverse mass of the trailing jet and $\rlap{E}{/}_T$, and (c) the transverse mass distribution of the W boson plus trailing jet. "Other" contains distributions too small to list individually, diboson, D-Y, and $t\bar{t}$.

XI. ACKNOWLEDGMENTS
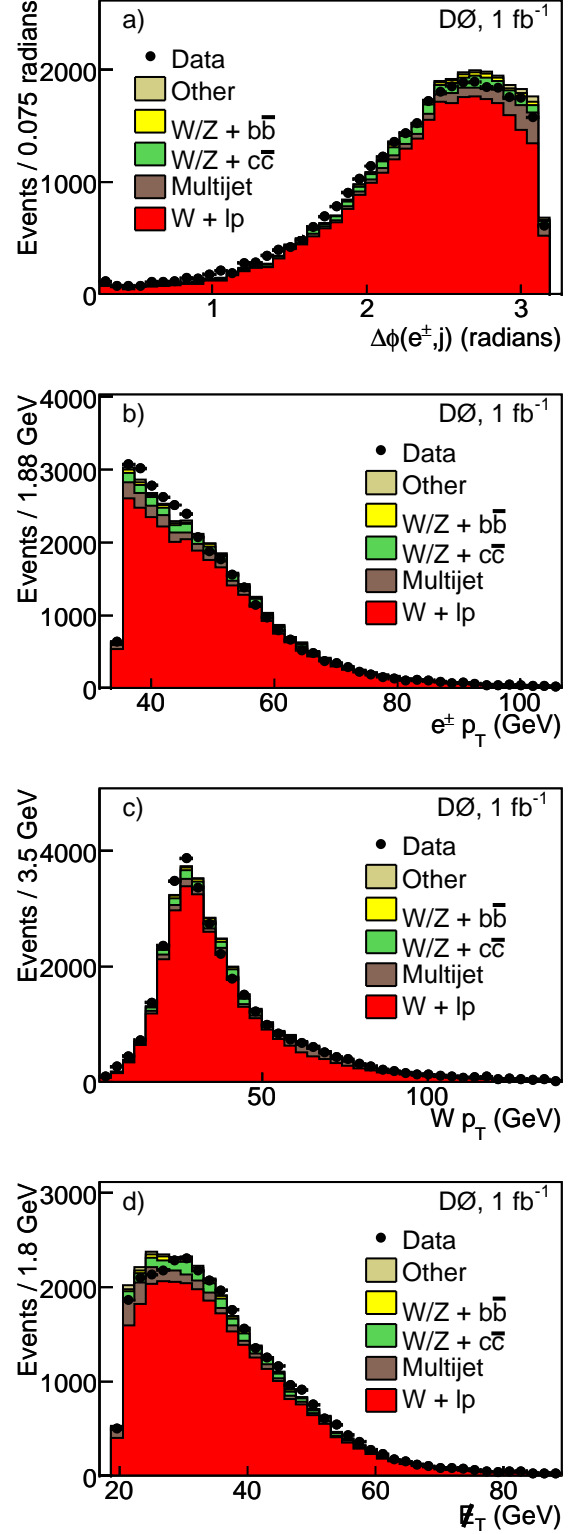
FIG. 15: (color online) The discrepant distributions in the $e + 1$ jet $+ \rlap{E}{/}_T$ exclusive final state. (a) The $\Delta\phi$ between the e and $\rlap{E}{/}_T$, (b) the p_T of the electron, (c) the p_T of the W boson, and (d) the $\rlap{E}{/}_T$ distribution. "Other" contains distributions too small to list individually, diboson, D-Y, and $t\bar{t}$.
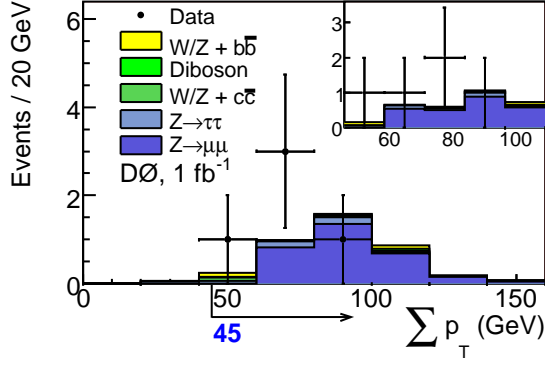
FIG. 16: (color online) Check of most discrepant CDF plots from [9], $\mu^{\pm}e^{\pm}$. The inset shows the distribution above the Σp_T cut.
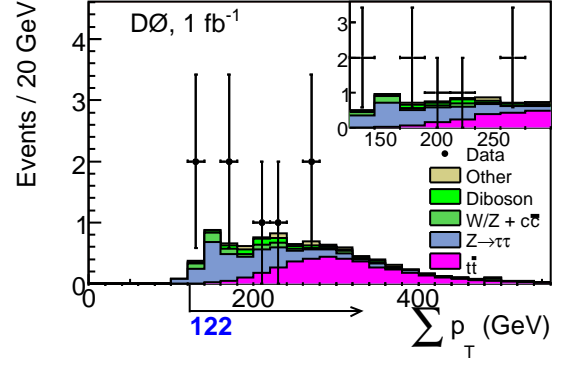

FIG. 19: (color online) Since there are no data events in the $\mu^{\pm} e^{\pm} + 2$ jets $+ \not\!\!E_T$ final state, the distribution for $\mu^{\pm} e^{\mp} + 2$ jets $+ \not\!\!E_T$ is shown. The inset shows the distribution above the Σp_T cut. "Other" contains the $Z \to \mu\mu$ and $W/Z + b\bar{b}$ distributions.
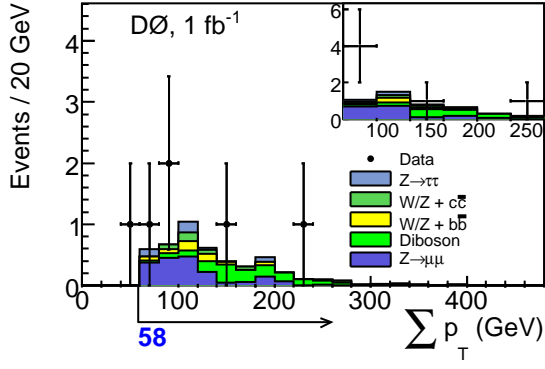

FIG. 17: (color online) Check of most discrepant CDF plots from [9], $\mu^{\pm}e^{\pm} + \not\!\!E_T$. The inset shows the distribution above the Σp_T cut.
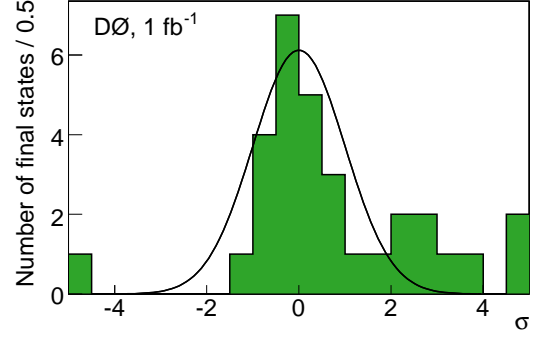

FIG. 20: (color online) Distribution of final state SLEUTH probabilities converted into units of σ before inclusion of the final state trials factor.
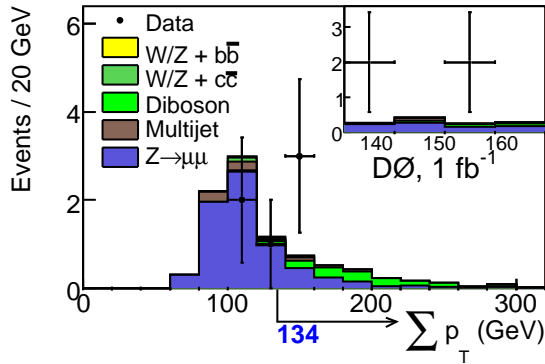

FIG. 18: (color online) Check of most discrepant CDF plots from [9], $\ell^{\pm}\ell^{\mp}\ell' + \not\!\!E_T$. The inset shows the distribution above the Σp_T cut.
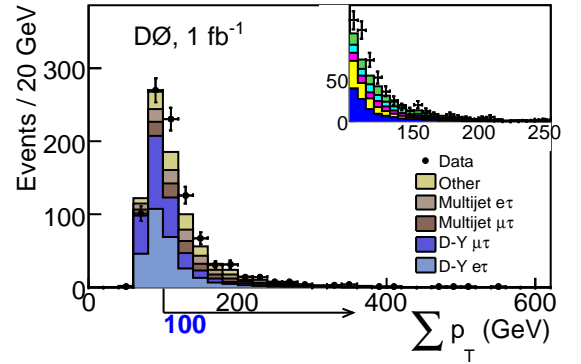

FIG. 21: (color online) SLEUTH plot for $\ell^{\pm} + \tau^{\mp} + \not\!\!E_T$. The inset shows the distribution above the Σp_T cut. "Other" includes D-Y $ee +$ jet events, D-Y $\mu\mu +$ jet events, diboson events, and $t\bar{t}$ events.

TABLE V: The SLEUTH states with $\tilde{\mathcal{P}} < 0.99$. The value of $\mathcal{P}$ represents the corresponding probability without taking into account the trial factor.

Final State	$\mathcal{P}$	$\tilde{\mathcal{P}}^a$
$\ell^+\ell^- + \not{E}_T$	$< 10^{-5}$	< 0.001
$\ell^\pm + 2\mathrm{j} + \not{E}_T$	$< 10^{-5}$	< 0.001
$\ell^\pm + \tau^\mp + \not{E}_T$	8.9×10^{-5}	0.0050
$\ell^\pm + \not{E}_T + 1\mathrm{j}$	0.00036	0.019
$e^\pm\mu^\mp + 2b + \not{E}_T$	0.0028	0.12
$\ell^\pm\tau^\pm + 2\mathrm{j} + \not{E}_T$	0.0028	0.12
$\ell^\pm + 2b + \not{E}_T$	0.0077	0.3
$e^\pm\mu^\mp + \not{E}_T$	0.0081	0.31
$\ell^\pm\tau^\pm$	0.057	0.91
$\ell^\pm + 2b + 2\mathrm{j} + \not{E}_T$	0.099	0.98

^{a} The value of $\tilde{\mathcal{P}}$ is not necessarily accurate below 0.001. The important check is whether the value drops below the threshold. Further discussion can be found in [8].

[1] T.P. Cheng and L.F. Li, Gauge Theory of Elementary Particle Physics (Oxford University Press, Oxford, UK, 2000).

[2] G.S. Guralnik, Int. J. Mod. Phys. A **24**, 2601, (2009).

[3] A. Zee, Quantum Field Theory in a Nutshell (Princeton University Press, Princton, NJ, 2003).

[4] D0 Collaboration, B. Abbott et al., Phys. Rev. Lett. **86**, 3712 (2001).

[5] D0 Collaboration, B. Abbott et al., Phys. Rev. D **62**, 092004 (2000).

[6] D0 Collaboration, V.M. Abazov et al., Phys. Rev. D **64**, 012004 (2001).

[7] H1 Collaboration, A. Aktas et al., Phys. Lett. B **602**, 14 (2004).

[8] CDF Collaboration, T. Aaltonen et al., Phys. Rev. D **78**, 012002 (2008).

[9] CDF Collaboration, T. Aaltonen et al., Phys. Rev. D **79**, 011101 (2009).

[10] D0 Collaboration, V.M Abazov et al., Nucl. Instrum. Methods Phys. Res. A **565**, 463 (2006).

[11] D0 Collaboration, V.M Abazov et al., Nucl. Instrum. Methods Phys. Res. A **552** 372 (2005).

[12] D0 Collaboration, V.M. Abazov et al., Phys. Rev. D **74**, 112004 (2006).

[13] D0 Collaboration, V.M Abazov et al., Phys. Lett. B **670**, 292 (2009).

[14] G. Blazey et al., in Proceedings of Physics at Run II: QCD and Weak Boson Physics Workshop: Final General Meeting, eds. U. Bauer, R. Ellis, arXiv: hep-ex/0005012 D. Zeppenfeld (Fermilab, Batavia, USA, 2000), p. 47.

[15] D0 Collaboration, V.M Abazov et al., Nucl. Instrum. Methods Phys. Res. A **620**, 490 (2010).

[16] M. Mangano et al., J. High Energy Phys. **07**, 001 (2003).

[17] T. Sjöstrand et al., J. High Energy Phys. **05**, 026 (2006).

[18] S. Hoeche et al, in Proceedings of HERA and the LHC: A Workshop on the implications of HERA for LHC physics: Part A, eds. A. De Roeck and H. Jung (CERN, Geneva, Switzerland, 2004), p. 288

[19] Z. Was, Nucl. Phys. **B**, Proceedings Supplements, **98** 96 (2001).

[20] D. J. Lange, Nucl. Instrum. Methods Phys. Res. A **462**, 152 (2001).

[21] Tevatron Electroweak Working Group, et al, arXiv:1107.5255 [hep-ex].

[22] R. Brun and F. Carminati, CERN Library Long Writeup, W5013, (1994).

[23] D0 Collaboration, V. M. Abazov et al., Phys. Rev. Lett. **101**, 241801 (2008).

[24] D0 Collaboration, V. M. Abazov et al., Phys. Rev. Lett. **102**, 051803 (2009).

[25] D0 Collaboration, V. M. Abazov et al., Phys. Rev. Lett. **100**, 102002 (2008).

[26] K. Melnikov and F. Petriello, Phys. Rev. D **74**, 114017 (2006).

[27] D0 Collaboration, V. M. Abazov et. al., Phys. Rev. Lett. **106**, 122001 (2011).

[28] S. Moch and P. Uwer, Phys. Rev. D **47**, 034003 (2008).

[29] J. Campbell and R. K. Ellis, Phys. Rev. D **65**, 113007 (2002).

[30] F. James, CERN Library Long Writeup, D506 (1998).

[31] D0 Collaboration, V.M. Abazov et al., Phys. Lett. B **705**, 200 (2011).

[32] T. Gleisberg et al., J. High Energy Phys. **02**, 056 (2004); T. Gleisberg, et al., J. High Energy Phys. **02**, 007 (2009).